Original paper

Age and tectonic setting of magmatic sulfide Cu–Ni mineralization in the Eastern Tianshan Orogenic Belt, Xinjiang, Central Asia

Chunming HAN[1,2*], Wenjiao XIAO[2,1], Guochun ZHAO[3], Benxun SU[1,3], Songjian AO[1], Jien ZHANG[1], Bo WAN[1]

[1] *Institute of Geology and Geophysics, Chinese Academy of Sciences, Beijing 100029, China; cm-han@mail.iggcas.ac.cn*
[2] *Xinjiang Research Center for Mineral Resources, Xinjiang Institute of Ecology and Geography, Chinese Academy of Sciences, Urumqi 830011, China*
[3] *Department of Earth Sciences, The University of Hong Kong, Pokfulam Road, Hong Kong, China*
[*] *Corresponding author*

During the Late Paleozoic, extensive magmatism and associated ore deposits were developed in the Eastern Tianshan Orogenic Belt (the Central Asian Orogenic Belt, NW China). In order to better constrain the petrogenesis of the intrusions in the area, we performed major- and trace-element whole-rock geochemical analyses as well as *in situ* zircon U–Pb and Hf isotopic analyses from the Xiangshan, Luodong and Poshi batholiths. Voluminous 276–284 Ma ultramafic and mafic rocks (associated with magmatic Cu–Ni sulfide deposits of the same age) have variable Hf isotopic compositions ($\varepsilon_{Hf}(t)$ = −10.3 to +14.3), indicating an origin via the contamination of depleted mantle-derived magma by variable amounts of ancient lower crust. The large mafic–ultramafic complexes were emplaced most likely during closure of the ancient Tianshan Ocean, resulting in the formation of several magmatic Cu–Ni sulfide deposits in the Early Permian times.

Keywords: Cu–Ni magmatic deposits; zircon SIMS U–Pb dating; Hf isotopes; petrogenesis; Eastern Tianshan Orogenic Belt; Central Asian Orogenic Belt
Received: 15 March 2013; accepted: 21 September 2013; handling editor: E. Jelínek

1. Introduction

The geochronological constraints on the magmatic events associated with orogenic processes contribute to a better understanding of the overall evolution of an orogen. Mafic magmatism may play a major role in extracting ore elements from the mantle. During the orogeny, these elements could be transported to the upper crust at economic concentrations.

The Eastern Tianshan Orogenic Belt (ETOB) covers an area of ~60,000 km^2, and is one of the important producers of Cu–Ni ores in China (Han et al. 2006). The ETOB ore cluster in the eastern Xinjiang consists of more than 50 metal deposits. In terms of metal associations, magmatic Cu–Ni sulfide deposits (Fig. 1) are the most important (Han et al. 2006). They all were genetically associated with the Late Paleozoic intrusive rocks (e.g. Mao et al. 2002; Zhou et al. 2004; Han et al. 2010).

The geodynamic setting and origin of the Late Paleozoic magmatism and associated Cu–Ni mineralization, however, remain controversial. Three contrasting models have been proposed for the mafic–ultramafic complexes in the Eastern Tianshan Orogenic Belt. They could 1) be a part of a Large Igneous Province (LIP) in the Tarim Craton, generated by a mantle plume (e.g. Zhou et al. 2004; Pirajno et al. 2008); 2) have resulted from post-collisional lithospheric delamination and asthenospheric upwelling, possibly related to slab-break off (Chai et al. 2008) or 3) have formed in a tectonic setting analogous to the Alaska-type zoned ultramafic complexes (e.g. Xiao et al. 2004b; Han et al. 2010).

The main objectives of this study are to establish the crystallization age of the magmatic Cu–Ni deposits of the ETOB and to constrain their genesis and geodynamic context. Such a study has important implications for Cu–Ni exploration potential of other mafic–ultramafic bodies in the region and, indeed, throughout much of the Central Asian Orogenic Belt (CAOB).

2. Geological background

The Eastern Tianshan Orogenic Belt, a part of the CAOB, contains a number of Paleozoic terranes, which accreted between the southern Siberian accretionary system to the North and the Tarim Craton to the South, and underwent a complex tectonic evolution (Coleman, 1989; Xiao et al. 2004a, b; Zhang et al. 2004; Zhou et al. 2004). The ETOB consists of four main tectonic units as follows (Fig. 1; Xiao et al. 2004b):

The *Dananhu–Tousuquan arc* composed of Ordovician to Devono–Carboniferous volcanic rocks, which mainly crop out along the southern edge of the Turpan–Hami Basin. The Devonian formations consist mainly of tholeiitic

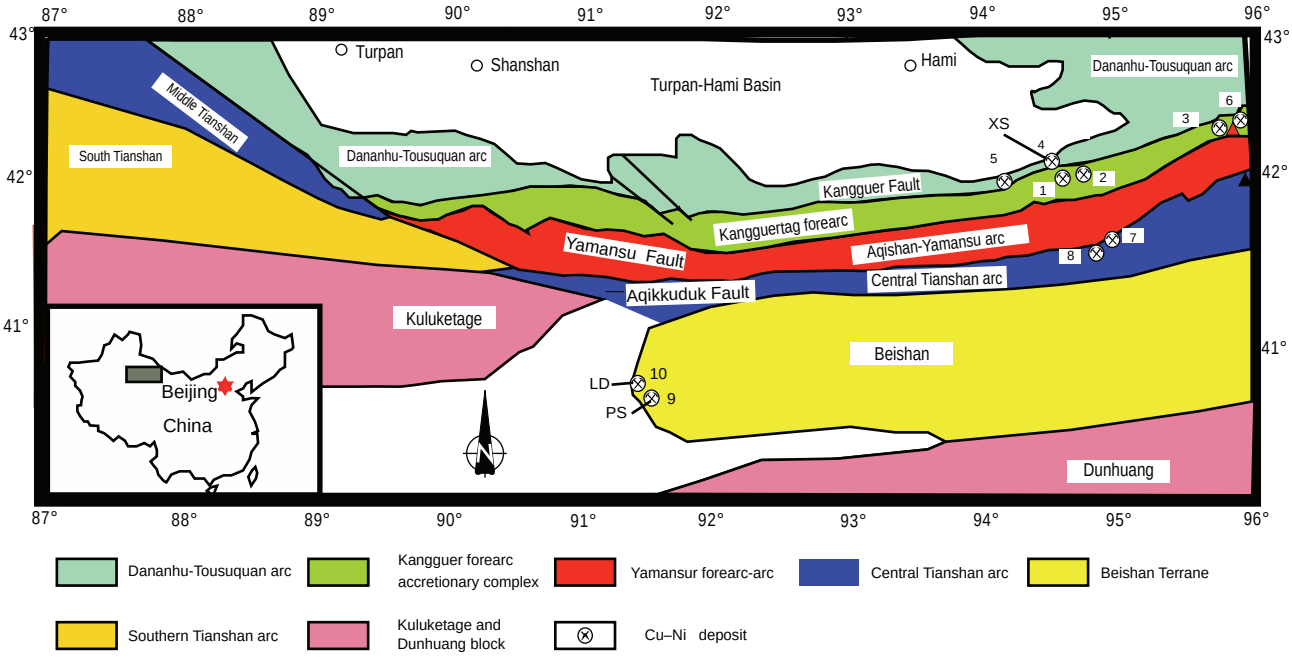

Fig. 1 Tectonic setting and distribution of significant mines of eastern Tianshan orogenic belt. Sample locations are also shown: XS – Xiangshan, LD – Luodong, PS – Poshi.

basalts, pyroclastic rocks, clastic sediments, and calc-alkali felsic lavas with tuffs; the Carboniferous formations consist predominantly of lavas, pyroclastic rocks, graywackes and carbonates (Yang XK et al. 1996, 2000; Zhou et al. 2001; Xiao et al. 2004b). Devonian–Carboniferous tholeiitic basalt and calc-alkaline andesite were interpreted to be island-arc related (Yang XK et al. 1996, 2000; Zhou et al. 2001). The SHRIMP zircon ages of 358 ± 7 Ma for a granodiorite and 383 ± 9 Ma for a granite (Song et al. 2002), indicate that the arc was Mid-Devonian to Early Carboniferous in age (Xiao et al. 2004b).

The *Kanggurtag forearc* accretionary complex contains submarine lavas and pyroclastic rocks that were thrust southward over the Yamansu forearc (Xiao et al. 2004b). The coherent strata include mainly Early–Middle Carboniferous volcano-sedimentary rock. The tholeiitic chemistry of volcanites in these formations suggests a forearc origin (Yang XK et al. 1996). Along the Kanggurtag Fault is an ultramafic–mafic complex several hundred kilometers long that was previously thought to be an ophiolite representing a consumed ocean based on geochemical and geological study (Ji JS et al. 1999, 2000; Zhou et al. 2001). The complex includes peridotite, lherzolite, gabbro, olivine gabbro, hornblende gabbronorite, pyroxene, and diorite. The zoned bodies intruded into, and were imbricated with, intensely deformed Devonian and Carboniferous strata. We view these rocks as analogous to the Alaska-type zoned ultramafic complexes in the Togiak arc in Goodnews Bay in southwestern Alaska (Xiao et al. 2004b). The SHRIMP zircon ages of 269.2 ± 3.2 Ma and 277.0 ± 1.6 Ma (Li JY et al. 2003) confirm that the ultramafic–mafic complex mainly formed in the Early Permian (Ji JS et al. 1999, 2000), contemporaneously with the eruptions of basic lavas and intrusions of granitic plutons in the area.

The *Yamansu forearc–arc* system is characterized by volcanic rocks and terrigenous clastic sediments interbedded with limestones (Xiao et al. 2004b). Devonian basalts–andesites are imbricated with slightly metamorphosed fine-grained clastics and carbonate, and overlain by the Carboniferous basalts–rhyolites. The Upper Carboniferous andesite and rhyolite are interbedded with clastic sediments and limestone. The andesite is calc-alkaline, whereas the basalt corresponds to an oceanic tholeiite (Ji JS et al. 2000). There is considerable Au and volcanogenic-hosted massive sulfide (VHMS) Cu–Fe mineralization in these arc rocks (Xiao et al. 2004b; Zhang et al. 2004). Ji JS et al. (1994) reported a Rb–Sr age of 300 ± 13 Ma and a Pb–Pb zircon age of 299 ± 16 Ma for rhyolites in these volcanic rocks. These dates are in good agreement with isotopic ages 290 to 300 Ma for volcanic rocks in the Yamansu area (Li HQ et al. 1998). All these isotopic ages indicate that subduction may have lasted to the Late Carboniferous; the Late Carboniferous arc magmatism moved seaward to the accretionary wedge. Permian volcanic sedimentary rocks are sparsely distributed above the arc; they are characterized by basalt and dacite (Xiao et al. 2004b). We interpret these Permian volcanic rocks as a continuation of the Devonian–Carboniferous arc.

The *Central Tianshan arc* system is located between the Aqikkuduk Fault to the north and the Kawabulak

Fault to the south (Xiao et al. 2004b). This unit has been regarded as a composite volcanic arc, composed of calc-alkaline basaltic andesite, volcanoclastics, minor I-type granite and granodiorite (Ma et al. 2012a, b). Its amphibolite-facies Precambrian basement consists of gneiss, quartz schist, migmatite and marble (Ma et al. 2013a, b). A volcano–sedimentary assemblage was identified including the Ordovician basalt–rhyolite, greywacke and the Silurian turbidite (Shu et al. 2002). Early Silurian and Early Carboniferous active margin sequences are widely exposed in the Central Tianshan magmatic arcs (Zhou et al. 2001). Silurian terrestrial clastic rocks with limestones are succeeded by Devonian limestones and terrestrial clastic rocks, overlain by Early Carboniferous volcanic rocks.

The *Beishan Terrane* is located in the northeastern part of the Tarim Basin, adjacent to the Central Tianshan arc in the north (Fig. 1). It is built mainly of Precambrian crystalline basement overlain by sedimentary rocks. The Precambrian to Permian strata in the Beishan region are separated by well-developed fault-related uplifts and sags (Su et al. 2012). Late Paleozoic tectonic evolution was closely related to the subduction and subsequent closure of the South Tianshan Ocean. The terrane developed in the Carboniferous–Permian times, accompanied by intermediate–basic volcanic eruptions (Su et al. 2012). The Permian mafic–ultramafic complexes discovered so far are predominately distributed in the western part of the Beishan terrane, and intruded the Proterozoic and Carboniferous sequences (Jiang et al. 2006; Su et al. 2012).

3. Geology of mineral deposits

In the ETOB, there are numerous mafic–ultramafic intrusions and related Cu–Ni deposits (Fig. 1; Han et al. 2013). In our study we focus on three of them that are located in two different tectonic units: the Dananhu–Tousuquan arc system (Xiangshan intrusion) and the Beishan rift terrane (Poshi and Luodong intrusions).

3.1. Xiangshan deposit

The Xiangshan Complex consists of the east, middle and west intrusions, 10.0 km long and up to 0.87 km wide, an outcrop of area of 2.8 km^2 (Fig. 2).

Several differentiated mafic–ultramafic intrusions have been identified in the complex, with an indicated and inferred resource of 20 000 t for 0.30 % Cu, and 40 000 t for 0.50 % Ni (Qin et al. 2003). The west Xiangshan intrusions (also called Xiangshanxi) in the western part of the deposit area are well differentiated, zoned, and mineralized with Cu–Ni and Ti–Fe.

The Xiangshanxi intrusion is oriented and elongated in a SW–NE direction. Is is of irregular shape, 4.25 km in length and 0.10–0.87 km in width, with a surface outcrop of 1.60 km^2. The pluton is a well-differentiated mafic–ultramafic body, consisting of gabbro, bojite and amphibole pyrolite units. The contacts between these units are generally transitional. The gabbro unit is distributed in the southern part of the mine and composed of (in vol. %) plagioclase (60–70), pyroxene (10–15) and hornblende (5–15). The bojite unit contains 25–45 vol. % of plagioclase, 15–40 % of pyroxene and 25–35 % of hornblende. The amphibole pyrolite unit consists of about 40–50 vol. % of olivine, 25–40 % of pyroxene and 10–20 % of hornblende.

The Xiangshan Complex contains more than ten major Cu–Ni sulfide ore bodies, divided into three types (Sun et al. 1996): (1) ore bodies that form beds and lenses at the bottom of the peridotite, pyroxenite, and gabbro zones. These ores are of low-grade, with Cu + Ni < 1 % and Cu/Ni < 1, and there is no distinct boundary between the ore bodies and wall rocks. (2) Orebodies that form lenses and veins at the contacts between gabbro–norite and hornblende peridotite and probably resulted from the injection of ore-bearing magma along zones of structural weakness. These ore bodies and wall rocks have clear-cut boundaries and the ore grade is Cu+ Ni >1 % with Cu/Ni >1. (3) Orebodies that occur as veins in fractures of various rock types, which consist of sulfide veinlets or sulfide-bearing quartz or carbonate veins and are small in size, with Cu + Ni ≈ 1 % and Cu/Ni > 1.

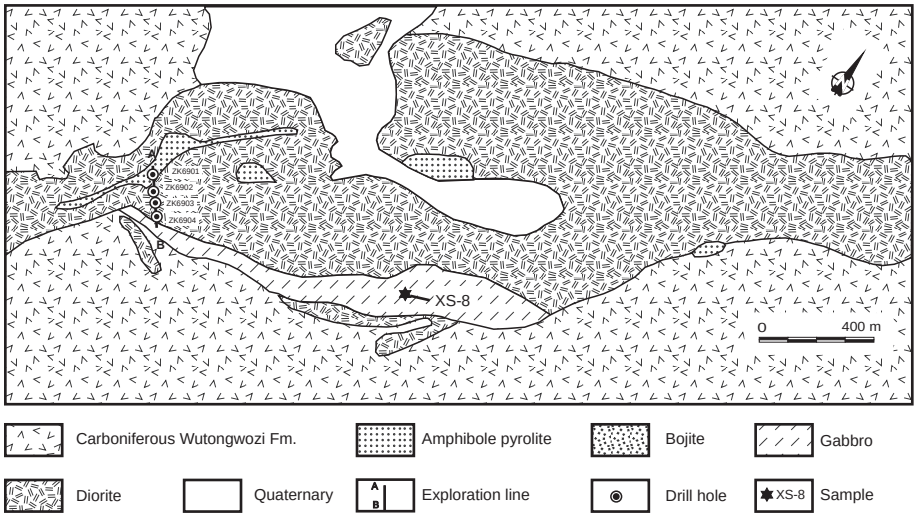

Fig. 2 Simplified geological map of Xiangshan deposit.

The Cu–Ni mineralization formed buried ore bodies in the western part of the No. 69 exploration line, primarily occurring as strata-bound ore deposits within the bojite unit and locally along the contact between the bojite and gabbro units (Fig. 2). There are two principal types: disseminated ores and massive ores. These ores are composed of pyrrhotite, pentlandite, violarite, cubanite, and chalcopyrite. Pyrrhotite and pentlandite are the major sulfides and commonly form euhedral or subhedral crystals.

According to mineral assemblages and crosscutting relationships of the ore-bearing veins, three mineralization stages can be identified (Sun et al. 1996). The first (magmatic crystallization stage) is characterized by disseminated ores, with pyrrhotite, pentlandite, chalcopyrite, pyrite, ilmenite and magnetite. The second (magmatic hydrothermal stage) is characterized by formation of the massive and vein, high-grade Cu and Ni ores, which overprint the disseminated ores. This ore assemblage consists of pyrrhotite, pentlandite, chalcopyrite, millerite, violarite, cubanite and marcasite. The third stage (supergene assemblage) is marked by supergene oxidation, which led to development of a thick gossan and formation of secondary minerals such as melanterite, chalcanthite, and gypsum.

3.2. Poshi deposit

The Poshi deposit is located in the Beishan rift zone (Fig. 1). It is underlain by Proterozoic basement rocks, mainly schists and migmatites, Lower Carboniferous pyroclastic rocks, Middle Carboniferous tuffs with marbles and Upper Carboniferous lavas (Fig. 3; Yang JQ et al. 2002). The Poshi Complex has an SW–NE elongated elliptical shape, ~2 × 1.6 km (~3.2 km^2). The two ultramafic bodies have distinct and similar zoning with gabbro → pyroxene peridotite → peridotite and dunite from the ore-bearing rock outward. The sulfide mineralization forms lenses, which more or less follow the shape of the lithological zones and dip toward the center of the complex at 22–80º (Fig. 3). The styles of the mineralization comprise net-textured, and injection veins of sulfide. Among main ore minerals rank pentlandite, chalcopyrite, pyrrhotite, magnetite, and chrome-spinel with very small amounts of vallerite, bornite, and millerite. The dominant gangue minerals include olivine, augite, enstatite, hornblende, phlogopite, and plagioclase. The ore minerals have euhedral–subhedral granular textures and are locally net-textured, forming mainly sparse disseminations, in places densely disseminated and massive. Grades range from 0.3 to 0.6 % Ni with maximum values of up to 0.96 %. The Cu and Co contents in the ores are low, generally below the cut-off grade, but locally where the Ni content >0.6 %, the Cu and Co grades rise above the cut-off grades. The Ni resources in the Poshi complex are

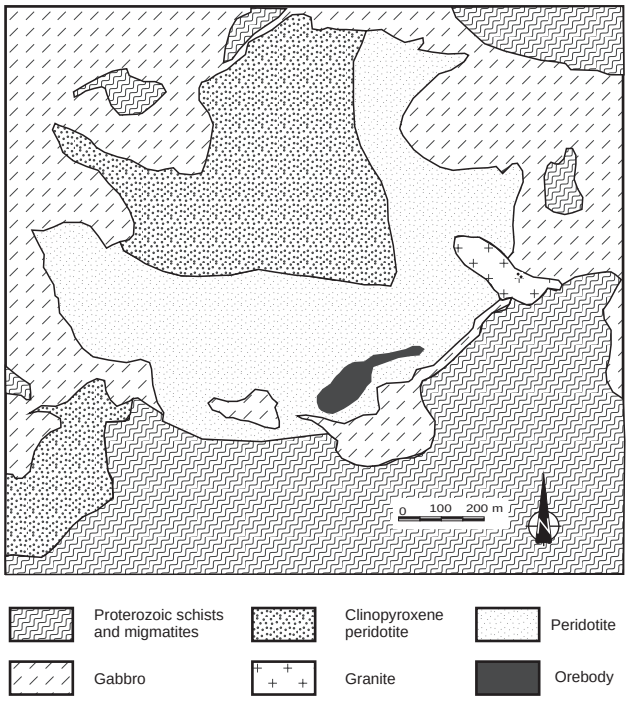

Fig. 3 Simplified geological map of Poshi deposit.

147,000 tons, but further exploration is ongoing (Mao et al. 2008).

3.3. Luodong deposit

The Luodong deposit is located west of the Poshi deposit and is 370 m long and 210 m wide (Fig. 4). The Luodong Complex consists of gabbro, olivine gabbro, peridotite, harzburgite, and pyroxenite. The ultramafic rocks were emplaced later than the gabbro. The N–S- and N–W-trending basic dykes intruded last. Sulphide mineralization is present in the peridotite. The ore bodies

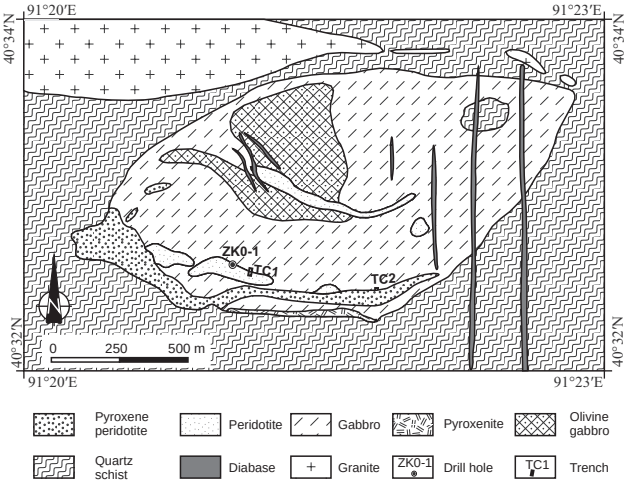

Fig. 4 Simplified geological map of Luodong deposit.

are 750–1060 m long with a thickness of 3.30–43.56 m. Three ore types, massive sulfide, disseminated and net-textured sulfide, are recognized. Chalcopyrite, pentlandite, and pyrrhotite are the dominant ore minerals in the sulfide ores. The currently indicated Ni metal resources are 57,200 t, grades range from 0.20 to 0.36 % Ni (Mao et al. 2008).

4. Analytical methods

Zircons were separated using conventional heavy liquid and magnetic techniques and picked under a binocular microscope. The grains were mounted along with Temora standard and then cast in epoxy resin in a 2.5 cm diameter mount and ground to expose the center of the grains. Internal structures of zircon were examined using cathodoluminescence (CL) images prior to U–Pb analyses. In-situ zircon U–Pb ages were acquired on the Cameca IMS-1280 ion microprobe (SIMS) in single collector mode at the Institute of Geology and Geophysics (IGG), Chinese Academy of Sciences, Beijing. The U–Th–Pb ratios and absolute abundances were determined relative to the standard zircon 91500 (Wiedenbeck et al. 1995), analyses of which were interspersed with those of unknown grains, using operating and data processing procedures similar to those described by Li XH et al. (2009). The mass resolution used to measure Pb/Pb and Pb/U isotopic ratios was 5400 during the analyses. A long-term uncertainty of 1.5% (1 RSD) for $^{206}Pb/^{238}U$ measurements of the standard zircons was propagated to the unknowns (Li QL et al. 2010), despite that the measured $^{206}Pb/^{238}U$ error in a specific session is generally around 1% (1 RSD) or less. Measured compositions were corrected for common Pb using non-radiogenic ^{204}Pb. Corrections are sufficiently small to be insensitive to the choice of common Pb composition, and an average of present-day crustal composition (Stacey and Kramers 1975) was used assuming that the common Pb is largely surface contamination introduced during sample preparation. Uncertainties on individual analyses in data tables are reported at a 1σ level; mean ages for pooled U/Pb (and Pb/Pb) analyses are quoted with 95% confidence interval. Data reduction was carried out using the Isoplot/Ex v. 2.49 program (Ludwig 2001).

In-situ Hf isotopic measurements of zircons were performed using a Neptune MC-ICP-MS, equipped with a 193 nm ArF Excimer laser at IGG. A spot size of 63 μm and a laser repetition rate of 10 Hz with pulse energy of 100 mJ/pulse were used for analyses. Detailed instrumental conditions, data acquisition, calibration and isobaric interference correction were described by Wu et al. (2006). During analyses, $^{176}Hf/^{177}Hf$ and $^{176}Lu/^{177}Hf$ ratios of standard zircon 91500 were 0.282294 ± 15 (2σ, n = 20) and 0.00031, respectively, which are similar to the $^{176}Hf/^{177}Hf$ ratio of 0.282306 ± 10, measured using the solution method (Woodhead et al. 2004) and the $^{176}Hf/^{177}Hf$ ratio of 0.282284 ± 22 by the laser ablation method (Griffin et al. 2006).

Five-kilogram samples for geochemical analyses were crushed using a ceramic jaw crusher, the resulting small chips were washed with distilled water and then powdered in an agate mortar. Major oxides were determined by X-ray Fluorescence (XRF) technique on fused glass beads using a Shimadzu XRF1500 sequential spectrometer at IGG. The analytical uncertainties are better than 5 % as revealed by long-term measurements of Chinese national standards GSR-1 and GSR-3.

Trace-element abundances were measured by Inductively Coupled Plasma Mass Spectrometry (ICP-MS) using a Finnigan MAT Element spectrometer at IGG. About 50 mg of crushed whole-rock powder was dissolved using HF/HNO_3 (10:1) mixtures in screw-top Teflon beakers for 7 days at ~100 °C, followed by evaporation to dryness, refluxing in 7 N HNO_3 to incipient dryness again, and the sample cake was then re-dissolved in 2% HNO_3 to a sample/solution weight ratio of 1 : 1 000. An internal standard was used for monitoring drift in mass response during mass spectrometric measurements; further details can be found in Gao et al. (2002).

5. Results

5.1. Zircon U–Pb geochronology

Three gabbro samples were taken for U–Pb dating: from the Xiangshan (XS, 94°33′45″E, 42°18′28″N), Poshi (PS, 91°30′12″E, 40°34′38″N) and Luodong (LD, 91°22′16″E, 40°33′26″N) intrusions. These gabbro samples exhibit intergranular texture, consisting of equivalent grains of clinopyroxene and plagioclase with minor olivine and hornblende. Clinopyroxene and plagioclase are present in roughly sub-equal amounts and together account for some 80 to 85 vol. % of the rock. Zircon U–Pb age data for the gabbro samples are listed in Tab. 1 and shown in the concordia diagrams. We consider each of the obtained ages to represent the best estimate of the crystallization age of the host gabbro, and, consequently, of the formation of the respective deposits.

Xiangshan intrusion: zircons are mostly small, euhedral and colorless. In CL images (Fig. 5a), no inherited cores were observed. They have high U (101–622 ppm) and Th (40–459 ppm) contents, and high Th/U ratios (0.40–0.95) (Tab. 1). Such features indicate that they crystallized from magmas (Wu et al. 2006). Fifteen analyses on 15 grains (Tab. 1) form a tight cluster on concordia

Tab. 1 SIMS U–Pb data for zircons from magmatic Cu–Ni deposits in East Tianshan, NW China

Sample spot	U (ppm)	Th (ppm)	Th/U	$f^{206\#}$ (%)	$^{207}Pb/^{206}Pb$	±1σ (%)	$^{207}Pb/^{235}U$	±1σ (%)	$^{206}Pb/^{238}U$	±1σ (%)	$t_{207/235}$ (Ma)	±1σ	$t_{206/238}$ (Ma)	±1σ
XS														
XS-1	294	203	0.69	0.13	0.0511	2.80	0.3125	3.28	0.0444	1.71	276.1	8.0	279.9	4.7
XS-2	126	79	0.63	0.26	0.0523	2.83	0.3178	3.21	0.0441	1.50	280.2	7.9	278.1	4.1
XS-3	622	459	0.74	0.03	0.0517	1.04	0.3194	1.96	0.0448	1.67	281.4	4.8	282.6	4.6
XS-4	302	210	0.69	0.36	0.0509	2.34	0.3140	2.79	0.0447	1.52	277.3	6.8	282.1	4.2
XS-5	160	95	0.59	0.17	0.0525	2.43	0.3167	3.11	0.0437	1.94	279.4	7.6	275.9	5.3
XS-6	101	40	0.40	0.26	0.0543	3.32	0.3257	3.65	0.0435	1.51	286.3	9.1	274.7	4.1
XS-7	229	149	0.65	0.13	0.0530	2.36	0.3269	2.83	0.0448	1.56	287.2	7.1	282.4	4.3
XS-8	238	184	0.78	0.31	0.0493	2.30	0.3000	2.81	0.0441	1.61	266.4	6.6	278.3	4.4
XS-9	234	96	0.41	0.09	0.0534	1.80	0.3251	2.34	0.0441	1.50	285.8	5.9	278.5	4.1
XS-10	373	259	0.69	0.16	0.0498	1.96	0.3015	2.65	0.0439	1.77	267.6	6.2	277.0	4.8
XS-11	112	65	0.58	0.33	0.0485	3.27	0.3036	3.60	0.0454	1.51	269.2	8.6	286.1	4.2
XS-12	185	120	0.65	0.11	0.0525	1.89	0.3197	2.46	0.0441	1.57	281.7	6.1	278.4	4.3
XS-13	413	459	1.11	0.14	0.0516	1.92	0.3126	2.54	0.0440	1.66	276.2	6.2	277.5	4.5
XS-14	304	214	0.70	0.05	0.0509	1.49	0.3149	2.13	0.0448	1.52	278.0	5.2	282.8	4.2
XS-15	340	324	0.95	0.02	0.0520	1.40	0.3204	2.13	0.0447	1.60	282.2	5.3	282.0	4.4
LD														
LD-1	1221	350	0.29	0.07	0.0521	0.91	0.3227	1.91	0.0453	1.65	284.0	4.7	285.9	4.6
LD-2	691	178	0.26	0.07	0.0525	0.98	0.3197	1.91	0.0446	1.59	281.7	4.7	281.2	4.4
LD-3	841	112	0.13	0.07	0.0521	0.92	0.3217	1.90	0.0453	1.62	283.2	4.7	285.4	4.5
LD-4	978	258	0.26	0.04	0.0519	1.15	0.3236	2.04	0.0455	1.66	284.7	5.1	287.1	4.7
LD-5	535	121	0.23	0.04	0.0523	1.12	0.3254	2.08	0.0451	1.75	286.1	5.2	284.5	4.9
LD-6	706	138	0.20	0.07	0.0524	1.02	0.3189	1.96	0.0446	1.63	281.0	4.8	281.2	4.5
LD-7	1111	269	0.24	0.06	0.0523	0.77	0.3256	1.84	0.0455	1.63	286.2	4.6	287.0	4.6
LD-8	961	177	0.18	0.05	0.0515	0.84	0.3165	1.81	0.0449	1.58	279.2	4.4	283.4	4.4
LD-9	657	170	0.26	0.11	0.0523	1.00	0.3180	1.98	0.0448	1.62	280.3	4.9	282.6	4.5
LD-10	909	168	0.18	0.04	0.0519	0.99	0.3208	1.91	0.0451	1.61	282.6	4.7	284.6	4.5
LD-11	817	164	0.20	0.05	0.0523	0.93	0.3210	2.01	0.0449	1.73	282.7	5.0	283.3	4.8
LD-12	1273	58	0.05	0.04	0.0519	1.12	0.3197	2.03	0.0450	1.67	281.7	5.0	283.5	4.6
LD-13	804	134	0.17	0.08	0.0522	1.09	0.3193	2.07	0.0449	1.71	281.3	5.1	283.1	4.7
LD-15	1001	257	0.26	0.11	0.0520	0.82	0.3193	1.88	0.0453	1.62	281.4	4.6	285.7	4.5
LD-16	869	179	0.21	0.05	0.0530	1.28	0.3271	2.14	0.0451	1.66	287.3	5.4	284.4	4.6
LD-17	1119	289	0.26	0.06	0.0522	0.77	0.3253	1.86	0.0457	1.67	286.0	4.7	287.8	4.7
LD-18	889	85	0.10	0.09	0.0519	0.88	0.3196	1.96	0.0453	1.71	281.6	4.8	285.4	4.8
PS														
PS10-1	889	389	0.44	0.28	0.0516	1.35	0.3122	2.07	0.0439	1.57	267.2	30.7	275.8	5.0
PS10-4	1031	283	0.27	0.26	0.0513	1.19	0.3073	2.07	0.0434	1.69	255.6	27.1	272.1	4.9
PS10-5	1298	461	0.36	0.08	0.0522	0.98	0.3157	2.04	0.0439	1.78	294.4	22.2	278.6	5.0
PS10-7	438	188	0.43	0.09	0.0512	1.40	0.3121	2.23	0.0442	1.74	249.9	31.8	275.8	5.4
PS10-8	568	358	0.63	0.92	0.0524	2.04	0.3067	2.57	0.0425	1.57	302.1	45.8	271.6	6.1
PS10-9	798	191	0.24	1.08	0.0506	1.92	0.3027	2.47	0.0434	1.56	222.0	43.9	268.5	5.9
PS10-10	1001	526	0.53	0.05	0.0519	1.13	0.3050	1.89	0.0426	1.52	282.6	25.6	270.3	4.5
PS10-11	562	174	0.31	0.12	0.0517	1.21	0.3231	2.00	0.0453	1.59	273.8	27.5	284.2	5.0
PS10-12	1238	211	0.17	1.31	0.0503	2.34	0.3159	2.81	0.0455	1.55	211.0	53.4	278.7	6.9
PS10-13	1021	549	0.54	1.51	0.0536	1.84	0.3126	2.50	0.0423	1.70	352.3	41.1	276.2	6.1
PS10-14	333	131	0.39	0.28	0.0505	1.94	0.3035	2.46	0.0436	1.50	217.1	44.4	269.1	5.8
PS10-15	476	166	0.35	0.21	0.0517	2.08	0.3139	2.64	0.0441	1.62	270.2	47.1	277.2	6.4

f206 is the percentage of common ^{206}Pb in total ^{206}Pb

and yield a weighted mean $^{206}Pb/^{238}U$ age of 279.6 ± 1.1 Ma (2σ, MSWD = 1.30, Fig. 6a).

Poshi intrusion: zircons are mostly small, euhedral and colorless lacking inherited cores (Fig. 5b). Zircons have high U and Th contents (333–1238 ppm and 131–461 ppm,

Fig. 5 Cathodoluminescence (CL) images of zircons from the Paleozoic mafic–ultramafic complexes in the Eastern Tianshan Orogenic Belt, NW China. Circles show the locations of SIMS U–Pb age isotope measurements, $^{206}Pb/^{238}U$ ages (Ma) and εHf(t) values are also shown above and below the circles, respectively. **a –** The Xiangshan gabbro, **b –** The Poshi gabbro, **c –** the Luodong gabbro. Numbers refer to spots listed in the Tab. 1.

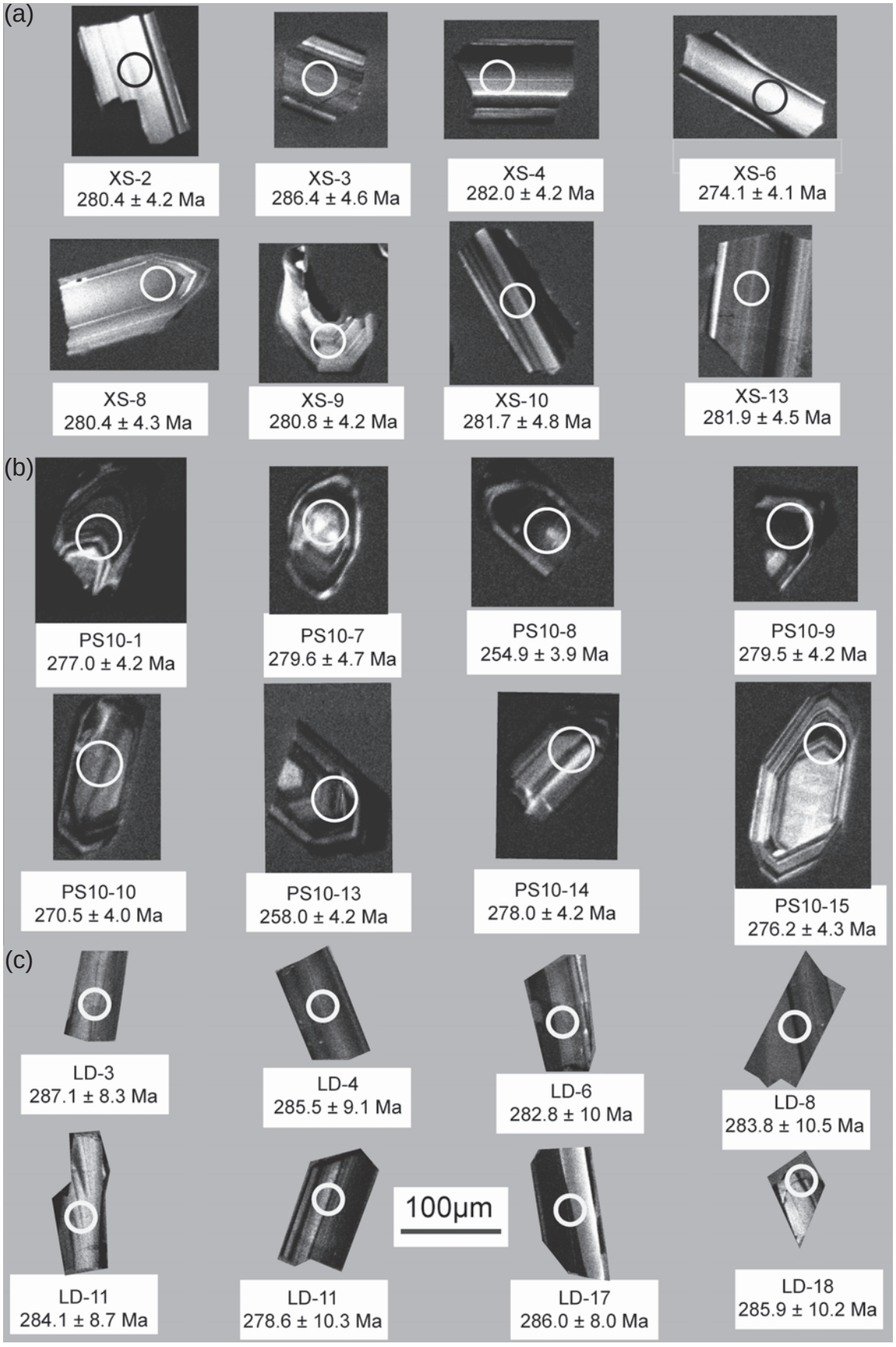
(a)
XS-2
280.4 ± 4.2 Ma
XS-3
286.4 ± 4.6 Ma
XS-4
282.0 ± 4.2 Ma
XS-6
274.1 ± 4.1 Ma
XS-8
280.4 ± 4.3 Ma
XS-9
280.8 ± 4.2 Ma
XS-10
281.7 ± 4.8 Ma
XS-13
281.9 ± 4.5 Ma
(b)
PS10-1
277.0 ± 4.2 Ma
PS10-7
279.6 ± 4.7 Ma
PS10-8
254.9 ± 3.9 Ma
PS10-9
279.5 ± 4.2 Ma
PS10-10
270.5 ± 4.0 Ma
PS10-13
258.0 ± 4.2 Ma
PS10-14
278.0 ± 4.2 Ma
PS10-15
276.2 ± 4.3 Ma
(c)
LD-3
287.1 ± 8.3 Ma
LD-4
285.5 ± 9.1 Ma
LD-6
282.8 ± 10 Ma
LD-8
283.8 ± 10.5 Ma
100μm
LD-11
284.1 ± 8.7 Ma
LD-11
278.6 ± 10.3 Ma
LD-17
286.0 ± 8.0 Ma
LD-18
285.9 ± 10.2 Ma

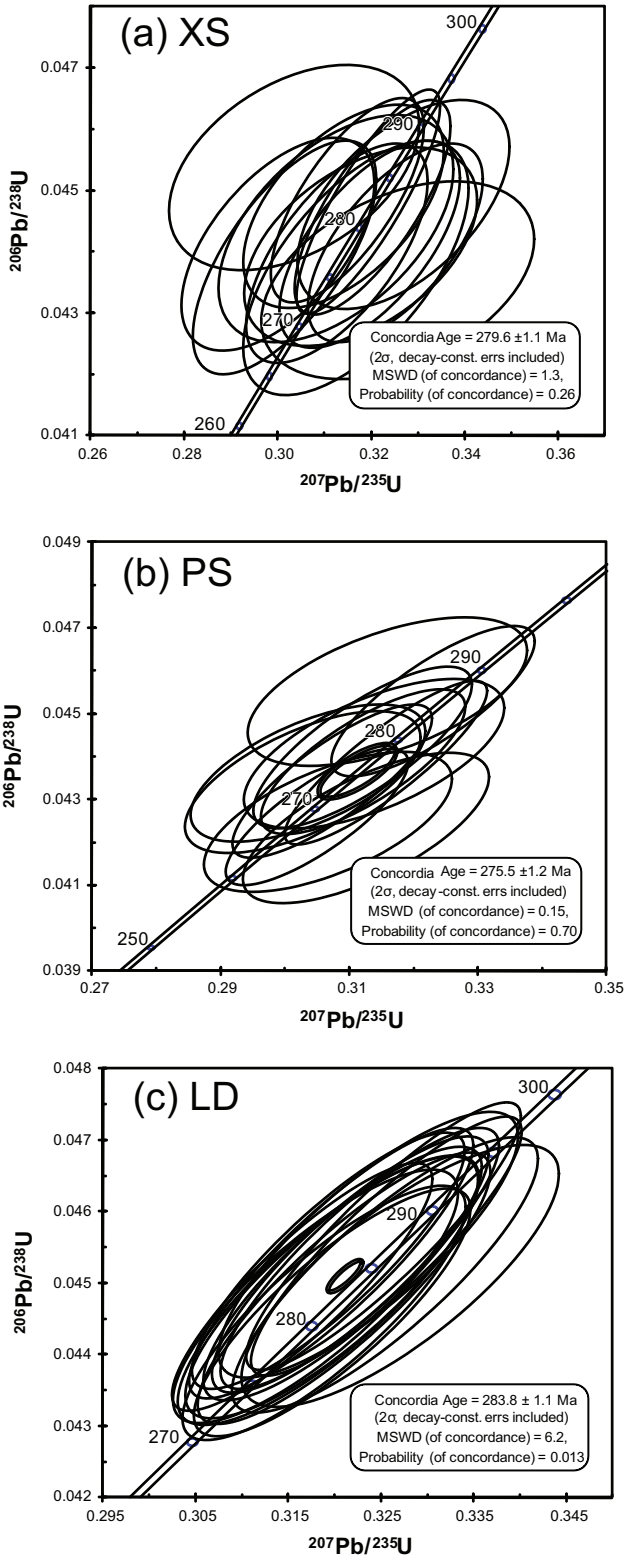

Fig. 6 Zircon U–Pb concordia diagrams for the dated Paleozoic mafic–ultramafic complexes in the Eastern Tianshan Orogenic Belt, NW China: **a –** The Xiangshan gabbro, **b –** The Poshi gabbro, and **c** –The Luodong gabbro.

respectively) and high Th/U ratios (0.17–0.63) (Tab. 1). Twelve analyses of 12 zircon grains (Tab. 3) form a tight cluster on concordia and yield a weighted mean $^{206}Pb/^{238}U$ age of 275.5 ± 1.2 Ma (2σ, MSWD = 0.15, Fig. 6b).

Luodong intrusion: zircons are mostly small and euhedral with no inheritance (Fig. 5c). They have high U (535–1221 ppm) and Th (58–350 ppm) contents, and corresponding Th/U ratios of 0.05–0.29 (Tab. 2). Seventeen analyses (Tab. 1) form a tight cluster on concordia and yield a weighted mean $^{206}Pb/^{238}U$ age of 283.8 ± 1.1 Ma (2σ, MSWD = 6.2, Fig. 6c).

5.2. Zircon Hf isotopic data

Zircon Hf analyses were undertaken on the same grains as those analyzed for U–Pb dating. Generally, where the grain or sub-domain was large enough, we ran the Hf analyses adjacent to the U–Pb spot; otherwise, we placed them on the top of the U–Pb data spot. We performed 60 Hf analyses on zircons from three intrusive rocks in the ETOB listed in Tab. 2.

Zircons from the Xiangshan gabbro have relatively uniform Hf isotope compositions ($^{176}Hf/^{177}Hf(t)$ = 0.28288–0.28298, $\varepsilon_{Hf}(t)$ = +10.0 to +13.3; average = +12.0) (Fig. 7), indicating that they were derived from a depleted mantle source that involved crust materials or an enriched mantle source.

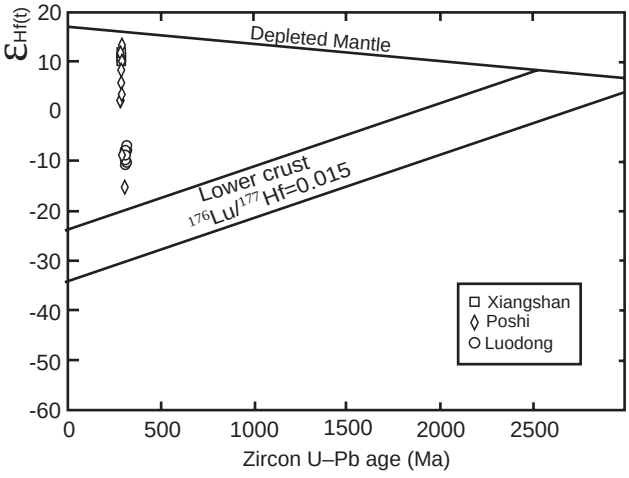

Fig. 7 Zircon U–Pb age versus εHf(t) diagram for the studied Eastern Tianshan mafic–ultramafic complexes.

Zircons from the Poshi gabbro have variable Hf isotope compositions ($^{176}Hf/^{177}Hf(t)$ = 0.28214–0.283004, $\varepsilon_{Hf}(t)$ = –16.2 to +14.3, indicating that the magma was derived from an asthenospheric depleted mantle and underwent variable degrees of crustal contamination. Zircons from the gabbro at Luodong are much more uniform in terms of their Hf isotope compositions ($^{176}Hf/^{177}Hf(t)$ = 0.28230–0.28238, $\varepsilon_{Hf}(t)$ = –10.5 to –7.7),

Tab. 2 Hf isotopic data for zircons from porphyry Cu and magmatic Cu–Ni deposits in East Tianshan

Samples	$^{176}Yb/^{177}Hf$	$^{176}Lu/^{177}Hf$	$^{176}Hf/^{177}Hf$	2σ	$(^{176}Hf/^{177}Hf)_i$	$\varepsilon_{Hf}0$	$\varepsilon_{Hf}t$	$T_{DM}1$	$T_{DM}2$	$f_{Lu/Hf}$
XS-8 01	0.038830	0.001590	0.282949	0.000016	0.282941	6.3	12.1	436	482	-0.95
XS-8 02	0.023289	0.000923	0.282955	0.000017	0.282950	6.5	12.5	420	465	-0.97
XS-8 03	0.029900	0.001215	0.282941	0.000016	0.282935	6.0	11.9	443	493	-0.96
XS-8 04	0.044419	0.001703	0.282924	0.000017	0.282915	5.4	11.2	474	531	-0.95
XS-8 05	0.053027	0.002156	0.282964	0.000017	0.282953	6.8	12.6	421	461	-0.94
XS-8 06	0.042300	0.001619	0.282889	0.000023	0.282881	4.2	10.0	522	593	-0.95
XS-8 07	0.028778	0.001154	0.282935	0.000018	0.282929	5.8	11.7	450	505	-0.97
XS-8 08	0.046036	0.001808	0.282948	0.000018	0.282938	6.2	12.0	441	489	-0.95
XS-8 09	0.040045	0.001629	0.282957	0.000015	0.282949	6.6	12.4	424	467	-0.95
XS-8 10	0.029460	0.001221	0.282943	0.000015	0.282936	6.0	12.0	441	491	-0.96
XS-8 11	0.035898	0.001460	0.282945	0.000019	0.282937	6.1	12.0	440	489	-0.96
XS-8 12	0.053895	0.002202	0.282987	0.000017	0.282975	7.6	13.3	388	417	-0.93
XS-8 13	0.038065	0.001550	0.282958	0.000014	0.282950	6.6	12.4	423	465	-0.95
XS-8 14	0.029238	0.001180	0.282926	0.000017	0.282920	5.4	11.4	465	522	-0.96
XS-8 15	0.023503	0.000964	0.282988	0.000019	0.282983	7.6	13.6	374	404	-0.97
XS-8 16	0.027973	0.001133	0.282945	0.000017	0.282939	6.1	12.1	437	487	-0.97
XS-8 17	0.029307	0.001187	0.282917	0.000016	0.282911	5.1	11.1	477	538	-0.96
XS-8 18	0.029045	0.001163	0.282951	0.000019	0.282945	6.3	12.3	429	475	-0.96
XS-8 19	0.020046	0.000819	0.282928	0.000016	0.282924	5.5	11.5	457	516	-0.98
XS-8 20	0.044773	0.001774	0.282953	0.000016	0.282944	6.4	12.2	432	477	-0.95
PS10 01	0.045397	0.001658	0.282781	0.000017	0.282772	0.3	6.1	680	764	-0.95
PS10 02	0.039688	0.001665	0.282978	0.000012	0.282970	7.3	13.0	395	420	-0.95
PS10 03	0.045640	0.001857	0.282908	0.000017	0.282899	4.8	10.5	498	544	-0.94
PS10 04	0.037522	0.001430	0.282685	0.000017	0.282677	-3.1	2.7	813	927	-0.96
PS10 05	0.039320	0.001614	0.282953	0.000019	0.282945	6.4	12.2	430	463	-0.95
PS10 06	0.047261	0.001923	0.282916	0.000016	0.282906	5.1	10.8	488	531	-0.94
PS10 07	0.039676	0.001638	0.283013	0.000017	0.283004	8.5	14.3	345	359	-0.95
PS10 08	0.050984	0.002052	0.282867	0.000016	0.282856	3.3	9.0	562	619	-0.94
PS10 09	0.049739	0.002165	0.282904	0.000021	0.282893	4.7	10.3	508	554	-0.93
PS10 10	0.035607	0.001482	0.282897	0.000014	0.282890	4.4	10.2	509	559	-0.96
PS10 11	0.046726	0.001958	0.282961	0.000017	0.282951	6.7	12.4	423	453	-0.94
PS10 12	0.040827	0.001742	0.283008	0.000015	0.282999	8.4	14.1	352	368	-0.95
PS10 13	0.033032	0.001205	0.282694	0.000019	0.282688	-2.8	3.1	795	907	-0.96
PS10 14	0.039994	0.001673	0.282915	0.000024	0.282907	5.1	10.8	486	529	-0.95
PS10 15	0.022027	0.000851	0.282378	0.000021	0.282373	-13.9	-8.0	1230	1444	-0.97
PS10 16	0.034996	0.001457	0.282932	0.000019	0.282924	5.7	11.5	459	498	-0.96
PS10 17	0.026884	0.001109	0.282668	0.000016	0.282662	-3.7	2.2	830	951	-0.97
PS10 18	0.047423	0.001978	0.282929	0.000020	0.282919	5.6	11.3	470	509	-0.94
PS10 19	0.036908	0.001344	0.282150	0.000019	0.282144	-22.0	-16.2	1566	1842	-0.96
PS10 20	0.052075	0.002093	0.282879	0.000017	0.282868	3.8	9.5	544	598	-0.94
LD 01	0.030194	0.000740	0.282347	0.000015	0.282343	-15.03	-8.9	1269	1558	-0.98
LD 02	0.097373	0.003406	0.282397	0.000017	0.282379	-13.27	-7.7	1290	1493	-0.90
LD 03	0.094134	0.003015	0.282356	0.000020	0.282340	-14.72	-9.1	1337	1563	-0.91
LD 04	0.125165	0.004322	0.282383	0.000017	0.282360	-13.75	-8.3	1345	1526	-0.87
LD 05	0.076086	0.002693	0.282319	0.000017	0.282305	-16.01	-10.3	1378	1626	-0.92
LD 06	0.105062	0.003709	0.282334	0.000017	0.282314	-15.50	-10.0	1396	1609	-0.89
LD 07	0.016770	0.000465	0.282371	0.000019	0.282369	-14.17	-8.0	1227	1512	-0.99
LD 08	0.103392	0.003658	0.282319	0.000022	0.282300	-16.01	-10.5	1416	1634	-0.89
LD 09	0.080523	0.002871	0.282348	0.000017	0.282332	-15.00	-9.3	1343	1576	-0.91
LD 10	0.074572	0.002677	0.282342	0.000015	0.282328	-15.21	-9.5	1345	1585	-0.92
LD 11	0.097022	0.003457	0.282369	0.000017	0.282351	-14.26	-8.7	1334	1544	-0.90
LD 12	0.061579	0.002241	0.282352	0.000016	0.282340	-14.84	-9.0	1314	1562	-0.93
LD 13	0.107024	0.003803	0.282328	0.000017	0.282308	-15.71	-10.2	1409	1620	-0.89
LD 14	0.114780	0.004030	0.282328	0.000019	0.282306	-15.71	-10.3	1418	1623	-0.88
LD 15	0.051986	0.001909	0.282350	0.000015	0.282340	-14.91	-9.1	1304	1563	-0.94
LD 16	0.086398	0.003065	0.282339	0.000017	0.282323	-15.30	-9.7	1363	1593	-0.91
LD 17	0.119604	0.004134	0.282391	0.000019	0.282369	-13.49	-8.0	1327	1511	-0.88
LD 18	0.061920	0.002240	0.282319	0.000017	0.282307	-16.01	-10.2	1361	1621	-0.93
LD 19	0.053480	0.001937	0.282350	0.000016	0.282340	-14.91	-9.1	1306	1563	-0.94
LD 20	0.094879	0.003400	0.282363	0.000019	0.282345	-14.46	-8.9	1340	1553	-0.90

Tab. 3a Major- and trace-element data of the Xiangshan deposit

Sample No.	HSB-71	HSB-31	HSB-68	HSB-85	HSB-58	HSB-61	HSB-81	HSB-84	HSB-60	HSB-57	HSB-75	HSB-53	HSB-82
Lithology	Hornblende gabbro								Gabbro	Amphibole–pyroxene peridotite			
SiO_2	45.69	48.27	46.62	47.29	46.47	45.39	45.39	46.12	50.26	41.25	43.44		44.66
TiO_2	1.10	0.40	1.07	0.91	1.42	1.43	1.58	0.88	0.75	0.43	0.60		1.81
AI_2O_3	18.51	15.82	18.99	20.67	11.58	9.12	9.56	7.98	7.45	8.41	8.84		9.88
Fe_2O_3*	10.75	6.29	10.47	8.26	11.65	11.98	12.16	11.70	8.69	13.83	11.45		13.34
MnO	0.14	0.12	0.09	0.09	0.18	0.19	0.17	0.13	0.18	0.16	0.16		0.17
MgO	6.41	10.19	6.19	6.20	10.89	15.59	15.16	17.96	13.65	22.39	22.61		14.98
CaO	10.35	12.46	10.48	10.71	12.58	12.18	11.77	10.40	15.89	5.84	6.63		11.09
Na_2O	3.41	2.99	3.23	2.88	2.04	1.47	1.55	1.21	1.57	0.57	0.70		1.62
K_2O	0.66	0.12	0.69	1.23	0.36	0.38	0.46	0.35	0.46	0.14	0.15		0.45
P_2O_5	0.48	0.04	0.71	0.37	0.51	0.86	0.54	0.36	0.15	0.05	0.06		0.25
LOI	2.48	2.38	1.28	1.42	1.75	1.00	1.30	2.70	0.85	6.43	5.45		1.30
Total	99.98	99.08	99.82	100.03	99.43	99.59	99.64	99.79	99.90	99.50	100.09		99.55
$Mg^{\#}$	70.26	86.52	70.08	74.84	78.74	83.76	83.16	85.88	86.16	86.51	88.67		81.65
La	16.79	3.10	20.39	12.78	17.08	23.77	17.77	30.79	12.09	2.93	3.39	2.97	15.74
Ce	45.59	6.33	48.68	31.24	48.29	79.09	57.51	56.09	35.03	6.04	8.11	5.94	54.22
Pr	7.66	1.11	7.69	5.12	7.99	14.28	10.25	6.76	5.69	1.06	1.40	0.99	10.14
Nd	37.74	5.52	36.54	24.80	37.01	70.62	50.47	26.52	25.97	5.04	6.74	4.52	53.13
Sm	8.48	1.45	7.65	5.91	8.40	14.95	11.48	4.67	5.5	1.30	1.84	1.22	12.88
Eu	2.27	0.56	2.15	1.78	2.21	3.49	2.77	1.32	1.48	0.44	0.58	0.41	2.93
Gd	7.44	1.57	7.10	5.35	7.41	11.89	9.93	3.85	4.76	1.45	2.01	1.31	11.99
Tb	1.09	0.26	0.95	0.77	1.08	1.57	1.36	0.52	0.70	0.25	0.35	0.23	1.77
Dy	5.97	1.61	4.87	4.09	5.48	7.68	6.88	2.57	3.60	1.53	2.15	1.36	9.43
Ho	1.14	0.34	0.86	0.77	1.06	1.43	1.34	0.47	0.70	0.32	0.44	0.29	1.85
Er	2.90	0.95	2.23	2.01	2.66	3.65	3.30	1.15	1.76	0.88	1.23	0.80	4.69
Tm	0.41	0.14	0.31	0.27	0.36	0.53	0.46	0.16	0.26	0.15	0.19	0.14	0.64
Yb	2.45	0.91	1.96	1.66	2.29	3.19	2.68	0.99	1.59	0.93	1.16	0.85	3.82
Lu	0.37	0.14	0.27	0.23	0.34	0.48	0.40	0.14	0.24	0.13	0.17	0.12	0.55
∑REE	140.65	24.00	141.65	96.80	141.65	26.60	176.57	135.99	99.35	22.44	29.77	21.14	183.80
(Eu/Eu)*	0.86	1.14	0.88	0.96	0.84	0.76	0.76	0.94	0.88	0.98	0.92	0.98	0.72
$(La/Yb)_N$	4.51	2.24	6.86	5.06	4.92	4.91	4.37	20.55	4.99	2.09	1.92	2.31	2.71
$(La/Sm)_N$	1.21	1.31	1.62	1.32	1.24	0.97	0.94	4.01	1.34	1.37	1.12	1.48	0.74
$(Gd/Yb)_N$	2.43	1.38	2.90	2.57	2.59	2.99	2.97	3.12	2.39	1.26	1.38	1.24	2.51
Sc	30	32	31	28	69	45	51	34	75	18	20	21	66
V	321	98	417	260	421	328	388	165	254	75	96	76	521
Cr	98	309	47	46	72	967	777	1350	939	1255	1423	1417	505
Co	33	35	38	29	44	56	56	73	39	160	96	88	64
Ni	53	74	68	49	105	311	290	685	163	3456	1053	648	258
Cu	15	66	69	54	143	259	209	55	41	5011	1294	288	58
Zn	84	37	62	64	101	117	112	104	74	176	97	78	119
Ga	25	11	29	25	18	18	18	12	12	7	9	7	19
Rb	7.5	0.2	9.1	14.9	1.9	0.7	0.8	1.2	4.9	1.4	1.3	1.3	0.9
Sr	1177	357	1351	1756	607	255	274	376	335	72	82	66	310
Y	28	9	25	19	24	35	31	11	17	8	12	8	43
Zr	81	24	51	41	63	75	77	128	57	33	35	30	77
Nb	4.5	1.3	4.2	3.5	6.4	11.2	8.2	9.7	4.7	1.7	1.9	1.4	8.1
Ba	216	61	216	801	91	82	90	166	222	10	15	8	94
Hf	2.6	0.7	1.9	1.5	2.6	3.4	3.0	3.1	2.3	0.9	1.1	0.8	3.5
Ta	0.17	0.07	0.25	0.16	0.26	0.43	0.32	0.56	0.21	0.11	0.12	0.08	0.30
Pb	1.7	1.9	2.6	1.7	1.6	0.8	1.4	1.5	0.9	2.3	1.1	0.6	0.9
Th	0.2	0.3	1.2	0.5	0.3	0.5	0.3	3.5	0.2	0.5	0.3	0.4	0.3
U	0.1	0.1	0.4	0.2	0.4	0.2	0.1	1.0	0.1	0.1	0.1	0.1	0.1

$Mg^{\#}$ = 100×Mg/(Mg + Fe) at. %; LOI = Loss on ignition

Tab. 3b Major- and trace-element data of the Poshi deposit

Sample No.	PSS01	PSS03	PSS04	PSS05	PSS06	PSS07	PSS08	PSS09	PSS10	PSS11	PSS12
Rock type	Olivine gabbro										
SiO_2	50.19	50.39	50.33	50.69	50.38	50.30	50.33	51.07	50.67	50.74	50.17
TiO_2	0.24	0.25	0.23	0.24	0.23	0.23	0.23	0.25	0.25	0.25	0.24
Al_2O_3	14.38	14.43	14.76	14.38	14.83	15.40	14.58	14.45	14.48	14.30	14.58
Fe_2O_3*	4.68	5.17	4.59	5.16	4.59	4.55	4.75	4.71	4.91	5.07	4.73
MnO	0.09	0.10	0.09	0.10	0.09	0.09	0.09	0.10	0.10	0.10	0.09
MgO	12.56	12.68	12.46	13.07	12.36	12.09	12.64	12.54	12.39	12.75	12.57
CaO	15.89	15.58	16.00	15.63	15.95	15.73	15.79	16.01	15.66	15.69	15.98
Na_2O	0.99	1.06	1.01	1.03	1.00	1.08	0.99	1.01	1.08	1.04	1.02
K_2O	0.05	0.05	0.05	0.04	0.05	0.05	0.05	0.05	0.05	0.05	0.05
P_2O_5	0.01	0.01	0.01	0.01	0.01	0.01	0.02	0.02	0.01	0.01	0.01
LOI	0.58	0.50	0.63	0.43	0.40	0.52	0.52	0.55	0.37	0.55	0.55
Total	99.67	100.22	100.17	100.80	99.89	100.04	99.99	100.76	99.96	100.55	100.01
$Mg^{\#}$	66	73	66	70	66	67	67	67	71	71	67
La	0.87	0.97	0.90	0.96	0.87	0.97	0.93	0.94	1.05	0.80	0.67
Ce	1.78	1.99	1.85	2.00	1.78	1.93	1.92	1.92	2.26	2.73	2.33
Pr	0.42	0.43	0.43	0.45	0.41	0.42	0.42	0.44	0.49	0.47	0.43
Nd	2.32	2.38	2.38	2.50	2.31	2.29	2.28	2.41	2.70	2.66	2.39
Sm	0.90	0.90	0.90	0.95	0.86	0.83	0.91	0.89	1.01	1.01	0.91
Eu	0.37	0.41	0.38	0.38	0.37	0.38	0.37	0.38	0.42	0.40	0.39
Gd	1.20	1.24	1.19	1.19	1.13	1.08	1.15	1.22	1.34	1.29	1.22
Tb	0.21	0.22	0.21	0.21	0.20	0.20	0.21	0.22	0.23	0.23	0.21
Dy	1.38	1.43	1.35	1.33	1.29	1.29	1.36	1.41	1.54	1.49	1.37
Ho	0.29	0.29	0.28	0.27	0.27	0.26	0.28	0.29	0.31	0.31	0.29
Er	0.74	0.75	0.75	0.73	0.73	0.71	0.75	0.77	0.84	0.83	0.77
Tm	0.10	0.11	0.10	0.10	0.10	0.10	0.11	0.11	0.12	0.12	0.11
Yb	0.61	0.62	0.63	0.62	0.61	0.57	0.63	0.66	0.71	0.69	0.64
Lu	0.09	0.10	0.09	0.09	0.09	0.08	0.09	0.09	0.10	0.10	0.09
∑REE	11.29	11.83	11.44	11.77	11.04	11.13	11.41	11.76	13.13	13.12	11.83
(Eu/Eu)*	0.91	0.85	0.90	0.91	0.88	0.83	0.92	0.89	0.90	0.93	0.89
$(La/Yb)_N$	0.96	1.05	0.97	1.03	0.96	1.12	1.00	0.96	1.00	0.78	0.71
$(La/Sm)_N$	0.61	0.67	0.63	0.63	0.63	0.74	0.64	0.67	0.66	0.50	0.45
$(Gd/Yb)_N$	1.57	1.60	1.52	1.54	1.48	1.48	1.47	1.49	1.52	1.50	1.54
Sc	46	48	46	45	44	43	44	46	48	43	44
V	127	125	125	125	122	117	121	126	136	132	128
Ga	9	10	10	9	10	10	9	9	11	9	9
Rb	1.0	1.1	1.1	0.9	1.1	1.1	1.1	1.0	1.1	0.9	0.6
Sr	178	185	191	178	182	188	177	176	195	187	185
Y	8	8	8	8	8	8	8	8	9	8	8
Zr	8	9	8	8	8	8	9	9	9	11	10
Nb	0.9	1.0	1.0	1.0	1.0	1.0	1.0	1.0	1.0	0.6	0.6
Ba	36	36	36	36	35	36	36	36	37	16	14
Hf	0.3	0.3	0.3	0.3	0.3	0.3	0.3	0.3	0.3	0.4	0.4
Ta	0.04	0.04	0.05	0.04	0.04	0.05	0.05	0.04	0.05	0.04	0.04
Pb	1.1	0.9	1.1	1.1	1.1	1.2	1.1	1.0	1.0	0.9	0.9
Th	0.07	0.07	0.09	0.07	0.08	0.10	0.10	0.08	0.09	0.11	0.08
U	0.04	0.04	0.05	0.04	0.04	0.05	0.05	0.04	0.05	0.01	0.01
Cr	809	789	1095	658	882	906	929	843	706	631	727
Co	36	42	3	38	34	34	35	34	40	40	37
Ni	172	252	195	182	184	169	181	172	189	166	170

$Mg^{\#}$ =100×Mg/(Mg + Fe) at. %; LOI = Loss on ignition

Tab. 3c Major- and trace-element data of the Luodong deposit

Sample No.	LD01	LD02	LD03	LD13	LD16	LD23	LD24	LD26	LD27	LD28	LD29	LD30	LD31	LD32
Rock type	Peridotite	Gabbro	Peridotite	Gabbro	Peridotite	Gabbro		Olivine gabbro					Gabbro	
SiO_2	39.89	52.08	39.59	52.11	40.22	52.33	50.83	47.03	48.33	48.24	49.07	47.75	50.08	50.12
TiO_2	0.16	0.40	0.27	0.38	0.25	0.42	0.37	0.43	0.32	0.34	0.34	0.30	0.43	0.43
Al_2O_3	5.38	17.04	6.54	18.04	4.57	17.35	18.05	18.26	18.77	18.04	19.35	18.80	16.97	17.35
Fe_2O_3*	11.10	5.74	10.87	5.28	10.49	5.71	5.48	5.56	5.62	5.80	4.98	5.68	5.65	5.72
MnO	0.14	0.11	0.14	0.10	0.13	0.11	0.09	0.09	0.08	0.09	0.08	0.08	0.10	0.10
MgO	35.15	11.79	31.98	10.75	35.50	11.45	11.39	11.07	12.37	12.66	11.16	12.74	11.78	11.41
CaO	2.69	9.63	3.55	9.88	3.47	10.49	9.15	10.88	10.36	10.43	10.58	10.28	10.28	10.21
Na_2O	0.64	2.17	0.61	2.31	0.60	2.24	2.26	5.01	2.26	2.29	2.45	2.16	2.28	2.55
K_2O	0.05	0.09	0.29	0.09	0.05	0.07	0.10	0.16	0.06	0.06	0.06	0.06	0.06	0.08
P_2O_5	0.02	0.03	0.03	0.03	0.03	0.03	0.03	0.04	0.03	0.03	0.03	0.03	0.04	0.04
LOI	4.76	1.77	5.53	1.95	4.35	0.62	2.28	2.20	2.60	2.70	2.72	2.86	2.76	2.53
Total	99.99	100.85	99.40	100.92	99.65	100.8	100.03	100.73	100.81	100.68	100.82	100.76	100.43	100.55
$Mg^{\#}$	56	87	61	88	53	89	86	90	81	82	80	79	85	89
La	1.08	1.01	0.79	0.96	0.41	1.01	1.11	1.32	0.83	0.93	0.95	0.93	1.12	1.26
Ce	2.45	3.20	2.51	3.03	1.90	3.26	3.11	3.88	2.76	2.59	2.65	2.59	3.27	3.61
Pr	0.35	0.57	0.45	0.53	0.39	0.58	0.52	0.67	0.50	0.52	0.53	0.51	0.63	0.68
Nd	1.56	2.85	2.38	2.70	2.18	3.04	2.64	3.45	2.68	2.77	2.66	2.64	3.20	3.46
Sm	0.47	0.96	0.80	0.90	0.78	1.02	0.89	1.15	0.91	0.93	0.88	0.88	1.10	1.15
Eu	0.21	0.52	0.29	0.51	0.28	0.55	0.49	0.54	0.45	0.49	0.51	0.47	0.58	0.55
Gd	0.54	1.16	0.99	1.11	0.94	1.27	1.01	1.41	1.12	1.16	1.09	1.07	1.36	1.45
Tb	0.10	0.21	0.18	0.20	0.17	0.23	0.18	0.25	0.20	0.21	0.19	0.19	0.25	0.26
Dy	0.66	1.40	1.16	1.33	1.13	1.53	1.22	1.63	1.32	1.40	1.29	1.29	1.67	1.73
Ho	0.14	0.31	0.26	0.29	0.24	0.33	0.27	0.34	0.28	0.30	0.27	0.27	0.37	0.37
Er	0.42	0.86	0.69	0.79	0.68	0.93	0.76	0.97	0.79	0.82	0.77	0.77	1.03	1.06
Tm	0.06	0.13	0.10	0.12	0.10	0.14	0.11	0.14	0.11	0.12	0.11	0.11	0.16	0.15
Yb	0.41	0.81	0.62	0.74	0.62	0.85	0.73	0.85	0.71	0.75	0.70	0.70	1.03	0.96
Lu	0.06	0.12	0.09	0.11	0.10	0.13	0.11	0.13	0.11	0.11	0.10	0.11	0.16	0.14
∑REE	8.51	14.11	11.29	13.31	9.90	14.84	13.15	16.72	12.76	13.08	12.71	12.52	15.93	16.84
(Eu/Eu)*	0.80	0.66	0.99	0.64	1.00	0.68	0.63	0.77	0.73	0.69	0.63	0.67	0.69	0.77
$(La/Yb)_N$	1.79	0.85	0.86	0.88	0.44	0.80	1.03	1.04	0.79	0.84	0.92	0.89	0.73	0.89
$(La/Sm)_N$	1.44	0.67	0.62	0.67	0.33	0.62	0.79	0.72	0.57	0.63	0.68	0.67	0.64	0.69
$(Gd/Yb)_N$	1.06	1.16	1.30	1.22	1.22	1.20	1.12	1.33	1.27	1.25	1.27	1.23	1.06	1.22
Sc	13	27	16	27	17	29	25	22	20	21	19	19	28	25
V	801	167	97	155	124	172	152	117	100	108	104	99	153	143
Ga	5	11	6	11	4	11	11	11	11	10	11	11	11	11
Rb	2.5	1.7	20.0	1.5	1.0	0.9	1.7	0.8	0.7	0.6	1.1	1.0	0.9	1.4
Sr	49	162	49	176	48	164	166	170	159	174	189	166	147	194
Y	4	8	9	8	7	9	7	9	8	8	7	7	9	9
Zr	13	26	21	24	20	26	22	30	22	21	21	20	28	28
Nb	0.9	0.7	0.7	0.7	0.6	0.7	0.7	0.7	0.6	0.7	0.7	0.7	0.7	0.8
Ba	26	31	50	30	21	30	31	28	26	30	31	31	34	34
Hf	0.4	0. 8	0.7	0.7	0.6	0.8	0.7	0.9	0.7	0.7	0.7	0.7	0.9	0.9
Ta	0.08	0.06	0.06	0.06	0.05	0.06	0.06	0.06	0.05	0.06	0.06	0.06	0.06	0.06
Pb	1.2	0.9	1.6	1.2	0.7	0.9	1.0	1. 1	0.9	0.9	0. 9	0.8	1.0	1.6
Th	0.6	0.2	0.3	0.1	0.1	0.2	0.1	0.2	0.1	0.1	0.1	0.1	0.2	0.2
U	0.13	0.05	0.05	0.07	0.01	0.03	0.08	0.05	0.02	0.03	0.03	0.03	0.13	0.16
Ni	1614	69	1397	70	1534	69	69	106	157	163	141	175	95	96
Cu	283	71	333	76	337	78	95	99	156	127	105	147	76	129
Co	116	35	110	33	113	35	33	38	43	46	40	50	35	42
Cr	3872	1009	4354	922	4507	1058	869	1029	1081	1087	966	970	1329	1196

$Mg^{\#}$ =100×Mg/(Mg + Fe) at. %; LOI = Loss on ignition

indicating that they were derived from a depleted mantle source that involved crustal materials or an enriched mantle source.

5.3. Major- and trace-element geochemistry

The mafic and ultramafic rocks hosting the Cu–Ni orebodies of the Xiangshan, Poshi and Luodong show a wide variation in their major oxide concentrations (Tab. 3). These samples have a wide range of SiO_2 (39.59–51.07 %, average 47.94 %), MgO (6.19–35.50 %, average 14.37 %) and Al_2O_3 (4.57–20.67 %, average 14.11 %), CaO (2.69–16.01 %, average 11.52 %) contents, but show relatively low TiO_2 (0.16–1.81 %, average 0.54 %) and $K_2O + Na_2O$ (0.65–5.17 %, average 1.94 %).

The diagrams of MgO versus major oxides and compatible elements exhibit evidence for the fractionation/accumulation of olivine, pyroxenes, and plagioclase. For example, a negative correlation of MgO with Al_2O_3, SiO_2, TiO_2 and CaO indicates fractionation/accumulation of olivine, pyroxenes and/or plagioclase; a positive correlation of MgO with compatible elements (e.g. Cr, Co and Ni) is consistent with fractionation/accumulation of olivine and orthopyroxene (Fig. 8).

All samples of Xiangshan have variable REE contents, reflecting different abundances and compositions of intercumulus liquids as well as distinct fractionation/accumulation histories, but are all enriched in LREE relative to HREE ($(La/Yb)_N$ = 1.92–20.55) and flat in the HREE segment ($(Gd/Yb)_N$ = 1.24–3.12) (Fig. 9a; Tab. 3a). Most of the samples show slightly negative or positive Eu anomalies (Eu/Eu*= 0.72 to 1.14), which may be attributed to the fractionation or accumulation of plagioclase, respectively. The patterns from Poshi intrusion are enriched in middle REE but show no LREE/HREE enrichment ($(La/Yb)_N$ = 0.71–1.00), while the Luodong patterns are more variable ($(La/Yb)_N$ = 0.44–1.79) (Fig. 9b–c; Tab. 3b–c). The Poshi and Luodong samples show small negative Eu anomalies (Eu/Eu* = 0.83–0.93 and 0.63–1.00, respectively).

The primitive mantle-normalized trace-element diagrams exhibit variable abundances of elements (Fig. 10), and most Xiangshan samples show pronounced negative Th, Nb, Ta, Pb, Zr and Hf anomalies, coupled with enrichments in Ba, U, La, Ce and Sr relative to their neighboring elements, which suggests chemical affinities with subduction-related rocks or continental crustal rocks (Fig. 10a). Other notable features of Poshi and Luodong samples include depletion of Th relative to Ba, enriched Pb and Sr relative to Ce and Nd, and depleted Zr relative to Nd (Fig. 10b–c). These patterns are similar to arc-related rocks (Chai et al. 2008).

6. Discussion

6.1. Geochronological framework

A large number of isotopic age data are available for magmatic Cu–Ni deposits in the ETOB. Most are whole-rock K–Ar or Sm–Nd ages; only a few were obtained by a Re–Os method (Han et al. 2013). Because of alteration, whole rock K–Ar and Sm–Nd ages provide poor constraints on the timing of the magmatism and mineralization in this area, though.

Recently, the intrusions of the ETOB have been dated by U–Pb SHRIMP and TIMS U–Pb methods on zircon (Rui et al. 2002; Han BF et al. 2004; Zhou et al. 2004; Chen et al. 2005; Jiang et al. 2006; Li HQ et al. 2006; Han CM et al. this volume). Despite these advances, the age distribution of igneous intrusions remains unclear due to the low density of sampling. Li HQ et al. (1998) suggested that the intrusive and ore-forming ages of the Huangshan and Huangshan East ore-hosting bodies are 309–305 and 320–314 Ma, respectively. Han BF et al. (2004) obtained a SHRIMP zircon U–Pb age of 274 ± 3 Ma for the Huangshan hyperite, while the associated diorite was emplaced at 269 ± 2 Ma (Zhou et al. 2004). Chen et al. (2005) presented a Re–Os isochron age of 283 ± 13 Ma for the Cu–Ni sulfide ores of the Hulu gabbro, newly dated at 282.3 ± 1.2 Ma by SIMS U–Pb on zircon (Han CM et al. this volume). Jiang et al. (2006) presented a SHRIMP zircon U–Pb age of 274 ± 4 Ma for the Poshi gabbro, within the error identical to our SIMS U–Pb zircon age of 275.5 ± 1.2 Ma. Li HQ et al. (2006) published a SHRIMP zircon U–Pb age of 278 ± 2 Ma for the Poyi gabbro. In addition, we have obtained a SIMS U–Pb zircon age of 283.8 ± 1.1 Ma from the Luodong gabbro.

Based on our and published zircon U–Pb ages, in combination with published Re–Os ages for Late Paleozoic intrusions and associated mineralization (Han CM et al. this volume) it can be concluded that the voluminous ultramafic–mafic rocks and associated Cu–Ni deposits in the ETOB have originated between late Carboniferous and Early Permian (256–300 Ma).

6.2. Metallogenic geodynamic mechanism

The ETOB is the easternmost segment of the Tianshan Mts. range in the southern Altaids, which extends eastwards through the Beishan Orogenic Belt to Inner Mongolia and occupies a key position between the central Asian belts to the west and east (Xiao et al. 2004b; Han CM et al. 2006). Its geodynamic evolution was closely linked with the development of an ancient Tianshan Ocean between the Tarim Block and Junggar–Kazakhstan Paleozoic active margin of the CAOB (Han and Zhao, 2003; Xiao et al. 2004b). The north Tianshan Ophiolitic

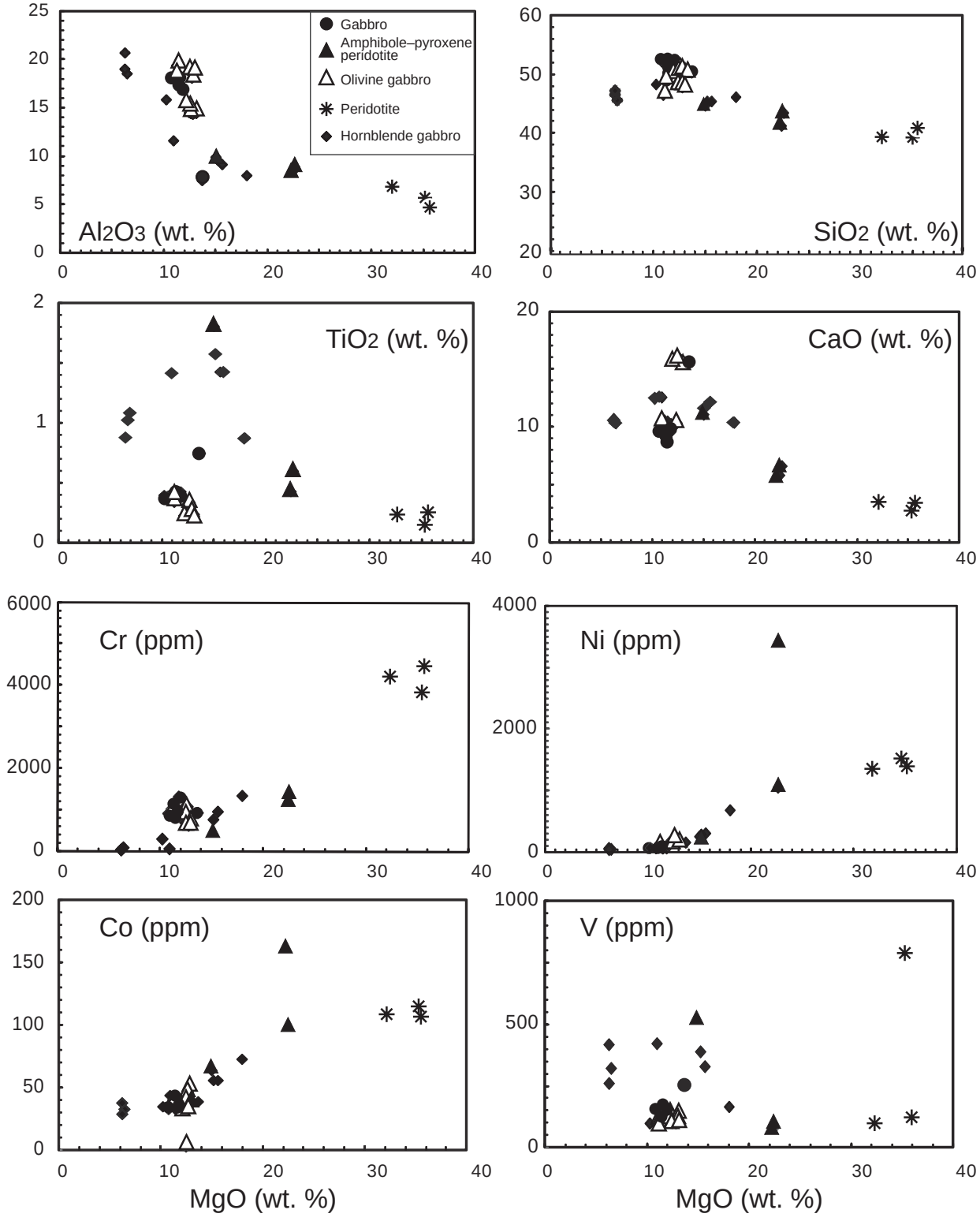

Fig. 8 Diagrams of MgO versus major oxides and compatible elements for the Xiangshan, Poshi and Luodong complexes.

Zone was the terminal suture zone of the CAOB in the Lower Permian. It triggered the destruction of the Tianshan Ocean and the collision of the accreted Junggar–Kazakhstan continental margin with the Tarim Block (Xiao et al. 2004b), leading to the formation of the Tianshan Orogen (Han and Zhao 2003). As was demonstrated above, the Cu–Ni mineralization in the east Tianshan occurred at *c.* 265–300 Ma.

The Early Permian zoned mafic–ultramafic complexes with Cu–Ni deposits in the ETOB are considered to be analogous to the zoned mafic–ultramafic intrusions in Alaska (Xiao et al. 2004b). In late Carboniferous to early Permian, the Beitianshan Ocean was consumed by northerly subduction beneath the Kangguertag arc–accretionary system (Xiao et al. 2010). The Tarim Craton probably have been in contact with its eastern Tien Shan end (promontory) with the arcs along the southern Siberian active margin, but leaving a remnant ocean (southern Tien Shan Ocean) (Xiao et al. 2010). In the meantime, the multiple arcs in the ETOB still had several subduction zones, and the Kanggurtag arc–accretionary system could have been interacting with this special active margin. The northerly Beitianshan Ocean could have had a ridge being subducted beneath this special active margin, generating the Alaskan-type mafic–ultramafic complexes in the Chinese eastern Tien Shan (Xiao et al. 2010). The setting could have resembled that in the southerly Kawabulake Ocean, resulting in emplacement of the Alaskan-type mafic–ultramafic complexes into the southwest tip areas of the Beishan, a joint effect of ridge-subduction and strike-slip faulting (Xiao et al. 2010).

The studied complexes in the Chinese East Tianshan are accompanied by coeval A-type granitic plutons (Zhang et al. 2004) as well as adakites and high-Mg andesites (Xiong et al. 2004), the latter comparable to the same rock association in Japan, Ecuador, Aleutians and California (Sisson et al. 2003; Windley et al. 2007). The production of these chemically distinct rocks is widely regarded as a blowtorch effect, as a result of the subduction of hot young crust at a ridge that creates a slab window through which upwelling mantle rises to trigger crustal anatexis and high-grade metamorphism in the forearc (Windley et al. 2007). In several places in this orogen, the upper amphibolite-facies belts are juxtaposed against greenschist-facies accretionary prisms (Wang and Wang 1992), as observed in the Jingerquan and Xiaoshitouquan belts (Wang et al. 1994). Such a juxtaposition of high- and low-grade metamorphic complexes is characteristic of modern accretionary orogens and can be interpreted as a result of ridge subduction (Brown 1998; Iwamori 2000; Windley et al. 2007). The

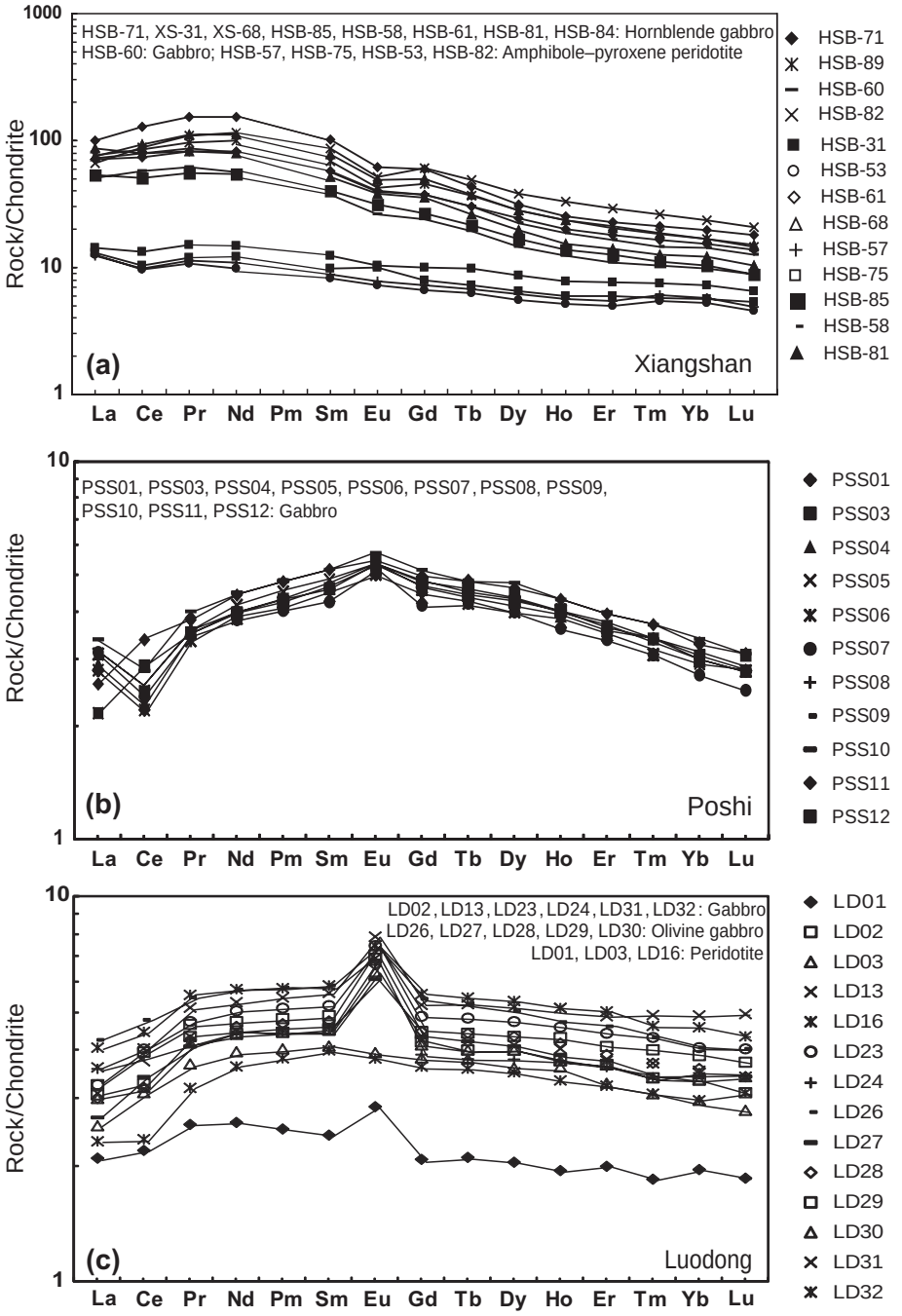

Fig. 9 Chondrite-normalized REE patterns from a suite of rocks of the Xiangshan (**a**), Poshi (**b**) and Luodong (**c**) complexes (normalizing values are from Sun and McDonough 1989).

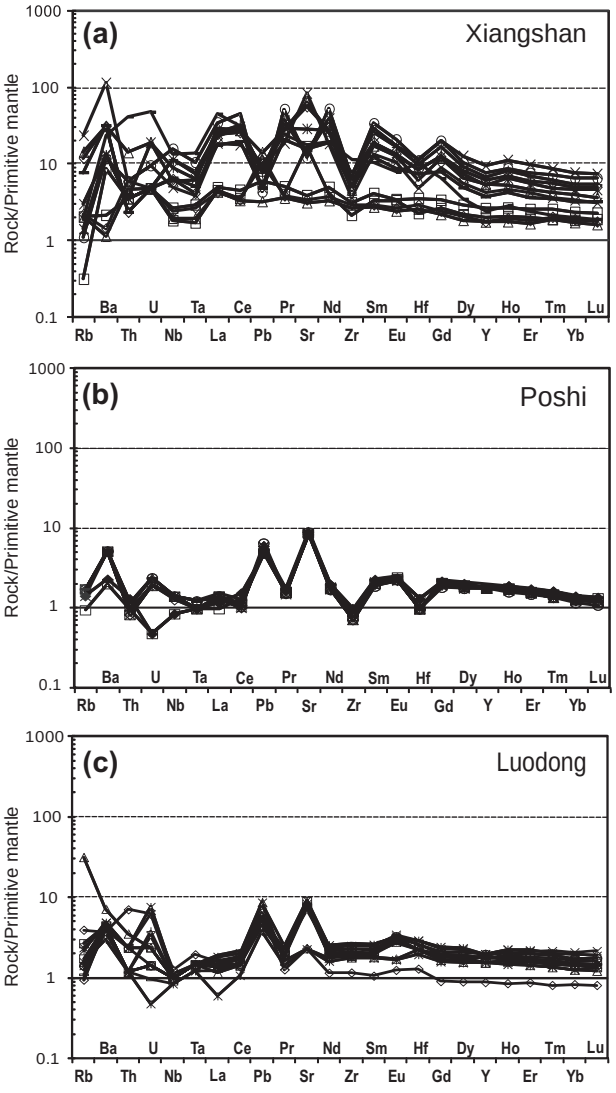

Fig. 10 Primitive mantle-normalized spidergrams for the three studied mafic–ultramafic complexes (normalizing values are from Sun and McDonough 1989).

eastern Tianshan orogenic type Au deposits are associated with Alaska-type Cu–Ni-bearing, zoned mafic–ultramafic bodies, and epithermal Au deposits were emplaced during syn- to post-accretionary times, followed by hydrothermal Au deposits (Zhang et al. 2004). These Au and Alaska-type Cu–Ni–PGE deposits in the Chinese East Tianshan most probably formed above a slab window created by a subducting ridge (Xiao et al. 2010), as those described in Alaska (Sisson et al. 2003). Such a mechanism can provide necessary heat (Windley et al. 2007).

7. Conclusions

Based on a combined *in situ* zircon U–Pb and Hf isotopic study of Late Paleozoic intrusions in the East Tianshan Orogenic Belt, NW China, we have reached the following conclusions.

(1) The geochronological data indicate that the rock and ore-forming events of the voluminous ultramafic–mafic complexes hosting the main Cu–Ni sulfide deposits in the East Tianshan Orogenic Belt occurred between late Carboniferous and Early Permian (276–284 Ma).

(2) Zircon Hf isotopic compositions show that the intrusions with the Cu–Ni deposits were derived from the same depleted mantle source but have experienced variable degrees of crustal contamination during the magma ascent.

(3) Based on available geological, geochemical and geochronological data, we suggest a model of ridge subduction as the best explanation for the petrogenesis of Cu–Ni deposits in the Chinese Tianshan Orogenic Belt.

Acknowledgements. We are indebted to Xianhua Li, Kezhang Qin and Lianchang Zhang for thoughtful discussions, which improved and initiated many of the ideas in this paper. We are grateful to Emil Jelínek, Jiří Zachariáš and an anonymous reviewer for their constructive comments on an early version of the manuscript, which led to its substantial improvement. This study was financially supported by funds from the National Natural Science Foundation projects (41230207, 41272107), the National 305 Project (2011BAB06B04–1), the One Hundred Talent Program B of the Chinese Academy of Sciences, the Chinese State 973 projects (2014CB440801, 2007CB411307) and Hong Kong RGC (7066/07P). This paper is a contribution to IGCP 592.

References

Brown M (1998) Ridge–trench interactions and high-T–low-P metamorphism, with particular reference to the Cretaceous evolution of the Japanese Islands. In: Treloar PJ, O'Brien PJ (eds) What Drives Metamorphism and Metamorphic Reactions? Geological Society of London Special Publications 138: pp 137–169

Chai FM, Zhang ZC, Mao JW, Dong LH, Zhang ZH, Wu H (2008) Geology, petrology and geochemistry of the Baishiquan Ni–Cu-bearing mafic–ultramafic intrusions in Xinjiang, NW China: implications for tectonics and genesis of ores. J Asian Earth Sci 32: 218–235

Chen SP, Wang DH, Qu WJ, Chen ZH, Gao XL (2005) Geological features and ore formation of the Hulu Cu–Ni sulfide deposits, Eastern Tianshan. Xinjiang Geol 23: 230–233 (in Chinese)

Coleman R (1989) Continental Growth of Northwest China. Tectonics 8: 621–635

Gao S, Liu XM, Yuan HL, Hattendorf B, Günther D, Chen L, Hu SH (2002) Determination of forty two major and

trace elements in USGS and NIST SRM glasses by laser ablation inductively coupled plasma-mass spectrometry. Geost Newsl 26: 191–196

Griffin WL, Pearson NJ, Belousova EA, Saeed A (2006) Comment: Hf-isotope heterogeneity in zircon 91500. Chem Geol 233: 358–363

Han BF, Ji JQ, Song B, Chen LH, Li ZH (2004) SHRIMP U–Pb zircon age of the mafic–ultramafic rocks and geological significance in Kalatongke and Huangshan, Xinjiang. Chin Sci Bull 49: 2324–2328 (in Chinese)

Han CM, Zhao GC (2003) Major types and characteristics of the Late Paleozoic ore deposits, east Tianshan, northwest China. Int Geol Rev 45: 798–814

Han CM, Xiao WJ, Zhao GC, Mao JW, Yang JM, Wang ZL, Yan Z, Mao QG (2006) Geological characteristics and genesis of the Tuwu porphyry copper deposit, Hami, Xinjiang, Central Asia. Ore Geol Rev 29: 77–94

Han CM, Xiao WJ, Zhao GC, Ao SJ, Zhang JE, Qu WJ, Du AD (2010) In-situ U–Pb, Hf and Re–Os isotopic analyses of the Xiangshan Ni–Cu–Co deposit in Eastern Tianshan (Xinjiang), Central Asia Orogenic Belt: constraints on the timing and genesis of the mineralization. Lithos 120: 47–562

Han CM, Xiao WJ, Zhao GC, Su BX, Sakyi PA, Ao SJ, Wan B, Zhang JE, Zhang ZY (2013) SIMS U–Pb zircon dating and Re–Os isotopic analysis of the Hulu Cu–Ni deposit, eastern Tianshan, Central Asian Orogenic Belt, and its geological significance. J Geosci 58: 255–274

Iwamori H (2000) Thermal effects of ridge subduction and its implications for the origin of granitic batholith and paired metamorphic belts. Earth Planet Sci Lett 181: 131–144

Ji JS, Tao HX, Zeng ZR, Li HQ, Zhang LC (1994) Geology of the Kanggurtag Gold Mineralization Zone and Exploration, East Tianshan. Geological Publishing House, Beijing, pp 1–136

Ji JS, Li HQ, Zhang LC (1999) Sm–Nd and Rb–Sr isotopic ages of magnetite–chlorite formation gold deposit in the volcanic rock area of Late Paleozoic Era, East Tianshan. Chin Sci Bull 44: 1801–1804 (in Chinese)

Ji JS, Yang XK, Liu GH (2000) Distribution of the gold and copper mineralization in Chol Tagh and their deposit prediction. Chinese National 305 Project 05–04: Urumqi, Xinjiang, China, pp 1– 593

Jiang CY, Cheng SL, Ye SF, Xia MZ, Jiang HB, Dai YC (2006) Lithogeochemistry and petrogenesis of Zhongposhanbei mafic rock body, at Beishan region, Xinjiang. Acta Petrol Sin 22: 115–126 (in Chinese)

Li HQ, Xie CF, Chang HL, Cai H, Zhu JP, Zhou S (1998) Study on Metallogenetic Chronology of Nonferrous and Precious Metallic Ore Deposits in North Xinjiang, China. Geological Publishing House, Beijing, pp 1–264 (in Chinese)

Li HQ, Chen FW, Mei YP, Wu H, Cheng SL, Yang JQ, Dai Y C (2006) Dating of the No. 1 intrusion of Pobei basic–ultrabasic rocks belt, Xinjiang, and its geological significance. Miner Depos 25: 463–469 (in Chinese)

Li JY, Xiao WJ, Wang KZ, Sun GH, Gao LM (2003) Neoproterozoic–Paleozoic tectonostratigraphic framework of Eastern Xinjiang, NW China, in Mao JW, Goldfarb R, Seltmann R, Wang DH, Xiao WJ, Hart C (eds) Tectonic Evolution and Metallogeny of the Chinese Altay and Tianshan, IGCP 473 Workshop 2003, Urumuqi, International Association on the Genesis of Ore Deposits (IAGOD), CERAMS/Natural History Museum, London, pp 31–74

Li QL, Li XH, Liu Y, Tang GQ, Yang JH, Zhu WG (2010) Precise U–Pb and Pb–Pb dating of Phanerozoic baddeleyite by SIMS with oxygen flooding technique. J Anal Atom Spec 25: 1107–1113

Li XH, Liu Y, Li QL, Guo CH, Chamberlain KR (2009) Precise determination of Phanerozoic zircon Pb/Pb age by multi-collector SIMS without external standardization. Geochem Geophys Geosyst 10: doi: 10.1029/cGC002400

Ludwig KR (2001) User's Manual for Isoplot/Ex rev. 2.49. Berkeley Geochronology Centre Special Publications 1a: pp 1–56

Ma XX, Shu LS, Santosh M, Li JY (2012a) Detrital zircon U–Pb geochronology and Hf isotope data from Central Tianshan suggesting a link with the Tarim Block: implications on Proterozoic supercontinent history. Precambr Res 206–207: 1–16

Ma XX, Shu LS, Jahn B-M, Zhu WB, Faure M (2012b) Precambrian tectonic evolution of Central Tianshan, NW China: constraints from U–Pb dating and in-situ Hf isotopic analysis of detrital zircons. Precambr Res 222–223: 450–473

Ma XX, Guo J, Liu F, Qian Q, Fan H (2013a) Zircon U–Pb ages, trace elements and Nd–Hf isotopic geochemistry of Guyang sanukitoids and related rocks: implications for the Archean crustal evolution of the Yinshan Block, North China Craton. Precambr Res 230: 61–78.

Ma XX, Shu LS, Santosh M, Li J (2013b) Paleoproterozoic collisional orogeny in Central Tianshan: assembling the Tarim Block within the Columbia Supercontinent. Precambr Res 228: 1–19

Mao JW, Yang JM, Qu WJ, Du AD, Wang ZL, Han CM (2002) Re–Os age of Cu–Ni ores from the Huangshandong Cu–Ni sulfide deposit in the East Tianshan Mountains and its implication for geodynamic processes. Miner Depos 21: 323–330 (in Chinese)

Mao JW, Franco P, Zhang ZH, Chai FM, Wu H, Chen SP, Cheng SL, Yang JM, Zhang CQ (2008) A review of the Cu–Ni sulfide deposits in the Chinese Tianshan and Altay orogens (Xinjiang Autonomous Region, NW China): principal characteristics and ore-forming processes. J Asian Earth Sci 32: 184–203

Pirajno F, Mao JW, Zhang ZC, Zhang ZH, Chai FM (2008) The association of mafic–ultramafic intrusions and A-type magmatism in the Tianshan and Altay orogens, NW China: implications for geodynamic evolution and potential for the discovery of new ore deposits. J Asian Earth Sci 321: 65–183

Qin KZ, Zhang LC, Xiao WJ, Xu XW, Yan Z, Mao JW (2003) Overview of major Au, Cu, Ni and Fe deposits and metallogenic evolution of the eastern Tianshan Mountains, Northwestern China. In: Mao JW, Goldfarb RJ, Seltmann R, Wang DH, Xiao WJ, Hart C (eds) Tectonic Evolution and Metallogeny of the Chinese Altay and Tianshan. IAGOD Guidebook Series 10: 227–249

Rui ZY, Goldfarb RJ, Qiu YM, Zhou TH, Pirajno F, Yun G (2002) Paleozoic–Early Mesozoic gold deposits of the Xinjiang Autonomous Region, Northwestern China. Miner Depos 37: 393–418

Shu L, Charvet J, Lu H, Laurent-Charvet S (2002) Paleozoic accretion–collision events and kinematics of deformation in the eastern part of the Southern–Central Tianshan Belt, China. Acta Geol Sin 76: 308–323 (in Chinese)

Sisson VB, Pavlis TL, Roeske SM, Thorkelson DJ (2003) Introduction: an overview of ridge–trench interactions in modern and ancient settings. In: Sisson VB, Roeske SM, Pavlis TL (eds) Geology of a Transpressional Orogen Developed During Ridge–Trench Interaction Along the North Pacific Margin. Geological Society of America Special Papers 371: pp 1–18

Song B, Li JY, Li WQ, Wang KZ, Wang Y (2002) SHRIMP dating of the Dananhu and Kezirkalasayi granitoid batholith in southern margin of Tuha Basin and their geological implications. Xinjiang Geol 20: 332–345(in Chinese)

Stacey JS, Kramers JD (1975) Approximation of terrestrial lead isotope evolution by a two-stage model. Earth Planet Sci Lett 26: 207–221

Su BX, Qin KZ, Sun H, Tang DM, Sakyi PA, Chu ZY, Liu PP, Xiao QH (2012) Subduction-induced mantle heterogeneity beneath Eastern Tianshan and Beishan: insights from Nd–Sr–Hf–O isotopic mapping of Late Paleozoic mafic–ultramafic complexes. Lithos 134–135: 41–51

Sun SS, McDonough WF (1989) Chemical and isotopic systematics of oceanic basalts: implications for mantle composition and processes. In: Saunders AD, Norry MJ (eds) Magmatism in the Ocean Basins. Geological Society London Special Publications 42: pp 313–345

Sun Y, Mu JL, Xiao YF (1996) The characteristics of shallow-rich ore body in copper–nickel sulphide deposit in Xiangshan, Xinjiang. J Miner Petrol 16: 51–57 (in Chinese)

Wang CY, Wang WB (1992) Characteristics and orogenic of the Kushui Metamorphic Belt in the eastern Tianshan Mountains. J Nanjing Univ 28: 595–604 (in Chinese)

Wang CY, Ma RS, Shu LS, Zhu WB (1994) Study on the regional metamorphism and the tectonic setting in the Eastern Tianshan Orogenic Belt. J Nanjing Univ 30: 494–503 (in Chinese)

Wiedenbeck M, Allé P, Corfu F, Griffin WL, Meier M, Oberli F, Von Quadt A, Roddick JC, Spiegel W (1995) Three natural zircon standards for U–Th–Pb, Lu–Hf, trace-element and REE analyses. Geost Newsl 19: 1–23

Windley BF, Alexeiev D, Xiao WJ, Kröner A, Badarch G (2007) Tectonic models for accretion of the Central Asian Orogenic Belt. J Geol Soc, London 164: 31–47

Woodhead J, Hergt J, Shelley M, Eggins S, Kemp R (2004) Zircon Hf–isotope analysis with an Excimer laser, depth profiling, ablation of complex geometries, and concomitant age estimation. Chem Geol 209: 121–135

Wu FY, Yang YH, Xie LW, Yang JH, Xu P (2006) Hf isotopic compositions of the standard zircons and baddeleyites used in U–Pb geochronology. Chem Geol 234: 105–126

Xiao WJ, Windley BF, Badarch G, Sun S, Li J, Qin K, Wang Z (2004a) Palaeozoic accretionary and convergent tectonics of the southern Altaids: implications for the growth of Central Asia. J Geol Soc, London 161: 339–342

Xiao WJ, Zhang LC, Qin KZ, Sun S, Li JL (2004b) Paleozoic accretionary and collisional tectonics of the Eastern Tianshan (China): implications for the continental growth of central Asia. Amer J Sci 304: 370–395

Xiao WJ, Mao QG, Windley BF, Han CM, Qu JF, Zhang JE, AO SJ, GUO QQ, CLEVEN NR, Lin SF, Shan YH, Li JL (2010) Paleozoic multiple accretionary and collisional processes of the Beishan orogenic collage. Amer J Sci 310: 1553–1594

Xiong XL, Cai ZY, Niu HC, Chen YB, Wang Q, Zhao ZH, Wu JH (2004) The late Paleozoic adakites in eastern Tianshan area and their metallogenetic significance. Acta Petro Sin 21: 967–976 (in Chinese)

Yang XK, Tao HX, Luo GC, Ji JS (1996) Basic features of plate tectonics in Eastern Tianshan of China. Xinjiang Geol 14: 221–227 (in Chinese)

Yang XK, Cheng HB, Ji JS, Luo GC, Tao, HX (2000) Analysis on gold and copper ore-forming setting with ore-forming system of Eastern Tianshan. J Xi'an Engin Univ 22: 7–14 (in Chinese)

Yang JQ, Zhong L, Deng G (2002) Metallogenic prognosis and prospecting targets of Pobei basic–ultrabasic rock bodies 1 and 10 in Beishan area. Xinjiang Geol 20: 214–218 (in Chinese)

Zhang LC, Xiao WJ, Qin KZ, Ji JS, Yang XK (2004) Types, geological features and geodynamic significances of gold–copper deposits in the Kanggurtag Metallogenic Belt, eastern Tianshan, NW China. Int J Earth Sci 93: 224–240

Zhou JY, Cui BF, Xiao HL, Chen SZ, Zhu D M (2001) The Kanggurtag–Huangshan collision zone of bilateral subduction and its metallogenic model and prognosis in Xinjiang, China. Volcanol Miner Resour 22: 252–263

Zhou MF, Lesher CM, Yang ZX, Li JW, Sun M (2004) Geochemistry and petrogenesis of 270 Ma Ni–Cu–(PGE) sulfide-bearing mafic intrusions in the Huangshan district, Eastern Xinjiang, northwestern China: implication for the tectonic evolution of the Central Asian Orogenic Belt. Chem Geol 209: 233–257